iScience

CellPress
OPEN ACCESS

Article

Ambient sunlight-driven photothermal methanol dehydrogenation for syngas production with 32.9 % solar-to-hydrogen conversion efficiency

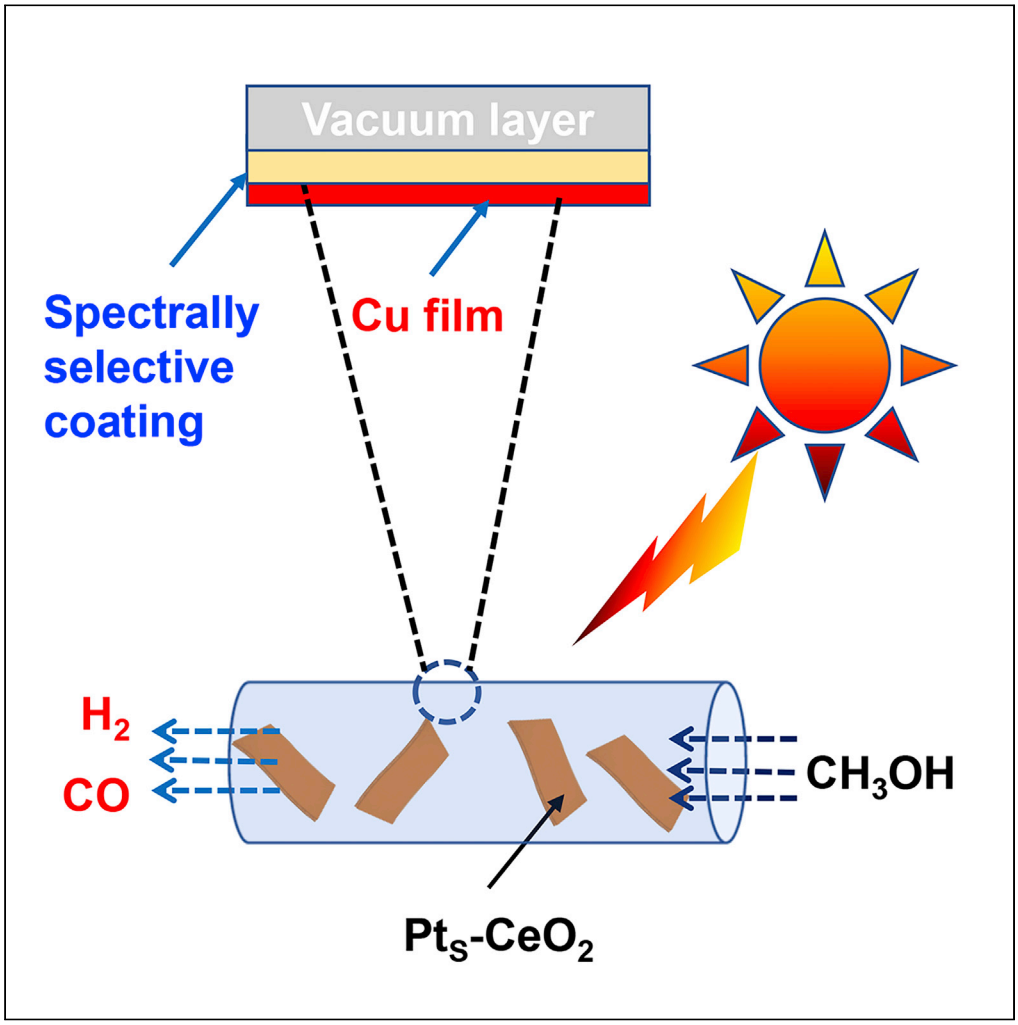

Xianhua Bai, Dachao Yuan, Yaguang Li, ..., Guangsheng Fu, Shufang Wang, Jinhua Ye

liyaguang@hbu.edu.cn (Y.L.)
song.hui@nims.jo.jp (H.S.)
jinhua.ye@nims.go.jp (J.Y.)

HIGHLIGHTS

Atomically substitutional Pt-doped CeO_2 is active and robust for CH_3OH dehydrogenation

The photothermal conversion device can heat Pt_s-CeO_2 to 299°C under 1 sun irradiation

The joint system achieves a one sun irradiated H_2 production rate of 481.1 mmol g^{-1} h^{-1}

This system delivers a high solar-to-H_2 efficiency of 32.9% under one sun irradiation

Bai et al., iScience 24, 102056
February 19, 2021
https://doi.org/10.1016/j.isci.2021.102056

iScience

CellPress
OPEN ACCESS

Article

Ambient sunlight-driven photothermal methanol dehydrogenation for syngas production with 32.9 % solar-to-hydrogen conversion efficiency

Xianhua Bai,[1,7] Dachao Yuan,[4,7] Yaguang Li,[1,*] Hui Song,[2,*] Yangfan Lu,[5] Xingyuan San,[1] Jianmin Lu,[6] Guangsheng Fu,[1] Shufang Wang,[1] and Jinhua Ye[2,3,8,*]

SUMMARY

Methanol dehydrogenation is an efficient way to produce syngas with high quality. The current efficiency of sunlight-driven methanol dehydrogenation is poor, which is limited by the lack of excellent catalysts and effective methods to convert sunlight into chemicals. Here, we show that atomically substitutional Pt-doped in CeO_2 nanosheets (Pt_s-CeO_2) exhibit excellent methanol dehydrogenation activity with 500-hr level catalytic stability, 11 times higher than that of Pt nanoparticles/CeO_2. Further, we introduce a photothermal conversion device to heat Pt_s-CeO_2 up to 299°C under 1 sun irradiation owning to efficient full sunlight absorption and low heat dissipation, thus achieving an extraordinarily high methanol dehydrogenation performance with a 481.1 mmol g^{-1} h^{-1} of H_2 production rate and a high solar-to-hydrogen (STH) efficiency of 32.9%. Our method represents another progress for ambient sunlight-driven stable and active methanol dehydrogenation technology.

INTRODUCTION

Owing to the intermittent nature of energy production by renewable sources such as wind and solar energy, the new method to store and transport energy is significant for sustainable industrial implementation of renewable energy technologies. Reversible energy storage in the form of stable and transportable chemicals like methanol can address these challenges (Govindarajan et al., 2020). Methanol dehydrogenation can produce syngas (a mixture of H_2 and CO) that has diverse applications (Dry, 2002; Khodakov et al., 2007). Syngas can not only contribute to electricity generation, transportation fuel production, and replacement for gasoline (Asthana et al., 2017; Paulino et al., 2020; Wang et al., 2020) but also serve as a vital chemical intermediate resource for the production of hydrogen via water-gas shift reaction, hydrocarbons via Fischer-Tropsch synthesis, ammonia via Haber-Bosch process, and higher chain alcohols/aldehydes via oxo-process (Huber et al., 2006). On the other hand, methanol dehydrogenation requires high operating temperatures due to the endothermic reaction nature, consuming a lot of energy restricting its application (Palo et al., 2007; Sordakis et al., 2018). As the most green and sustainable energy, solar-driven hydrogen generation from methanol is an attractive strategy to save the nonrenewable energy while storing solar energy (Huang et al., 2019; Liu et al., 2016, 2018; Wang et al., 2018b). So far, the efficiency of sunlight-driven methanol dehydrogenation via photocatalytic and photothermal synergistic strategies is difficultly improved due to the limitations in photogenerated carriers' transfer (Liu et al., 2016), sunlight absorption, and reactivity (Chen et al., 2010; Kudo and Miseki, 2009; Xiao and Jiang, 2019). As far as we known, the state of the art of sunlight-driven hydrogen production rate from methanol dehydrogenation is ~0.2 mmol g^{-1} h^{-1} (Pang et al., 2019), far behind the demands of industrialization. Therefore, it is a great challenge to develop an innovative and sustainable solar-driven system that is highly efficient, stable, and low-cost to generate H_2 and CO from methanol without additional energy input.

Except photocatalytic and photothermal synergistic strategies (Chai et al., 2016; Wang et al., 2018c), directly converting sunlight into thermal energy to drive catalytic reactions, namely sunlight-driven thermal catalysis, is another promising route to efficiently store solar energy into chemicals (Li et al., 2019; O'Brien et al., 2018), as black materials can absorb almost all the sunlight, from UV to infrared (IR) light, and convert it to thermal energy (Bae et al., 2015; Oara Neumann et al., 2013). However, the temperatures of black materials under natural sunlight irradiation are usually lower than 100°C due to the serious dissipation of

[1]Hebei Key Lab of Optic-electronic Information and Materials, The College of Physics Science and Technology, Institute of Life Science and Green Development, Hebei University, Baoding 071002, P. R. China

[2]International Center for Materials Nanoarchitectonics (WPI-MANA), National Institute for Materials Science (NIMS), 1-1 Namiki, Tsukuba, Ibaraki 305-0044, Japan

[3]TJU-NIMS International Collaboration Laboratory, School of Material Science and Engineering, Tianjin University, Tianjin 300072, P. R. China

[4]College of Mechanical and Electrical Engineering, Hebei Agricultural University, Baoding 071001, P. R. China

[5]School of Materials Science and Engineering, State Key Laboratory of Silicon Materials, Zhejiang University, Hangzhou 310027, P. R. China

[6]State Key Laboratory of Catalysis, Dalian Institute of Chemical Physics, Chinese Academy of Sciences, 457 Zhongshan Road, Dalian 116023, P. R. China

[7]These authors contributed equally

[8]Lead contact

*Correspondence: liyaguang@hbu.edu.cn (Y.L.), song.hui@nims.jo.jp (H.S.), jinhua.ye@nims.go.jp (J.Y.)

https://doi.org/10.1016/j.isci.2021.102056

thermal energy (Xu et al., 2017; Zeng et al., 2014), making it difficult to initiate methanol dehydrogenation (requiring 200°C to drive this reaction) (Brown and Gulari, 2004; Marbán et al., 2010; Mostafa et al., 2009). Our recent work of using selective light absorber to construct a photothermal conversion system is able to convert dispersed solar energy to high temperature (~288°C), which provides the potential of realizing natural sunlight-driven methanol dehydrogenation reaction (Li et al., 2019). Additionally, exploring efficient and stable catalysts to produce hydrogen from methanol dehydrogenation at mild operating temperatures is also crucial. Recently, single-atom catalysts have shown extraordinary activities in various reactions, e.g., CO_2 reduction (Yang et al., 2018; Zhao et al., 2017), oxygen reduction reaction (Chen et al., 2017), ethanol oxidation (Wang et al., 2017), owing to the maximum atom-utilization efficiency and unique electronic features. In order to make single-atom catalysts practical, the preparation of single atoms with high loading amounts is a basic factor. However, the dense single atoms in thermal catalysis are generally not stable under realistic reaction conditions due to their active nature (Qiao et al., 2011; Wei et al., 2014). Exploring highly stable and active dense single atom catalysts are thus the key to achieve practical solar-driven hydrogen generation from methanol.

In this work, in order to achieve efficient methanol dehydrogenation with high STH conversion efficiency under only one sun irradiation, we first developed a bimetal metal ions adsorption strategy to synthesize Pt single atoms on CeO_2 nanosheets (Pt_s-CeO_2) with a high Pt content (7.4 at%) and a lattice substituted single atom structure. The experimental and theoretical results evidently showed that lattice confinement strategy leads to both high activity and robust structure stability for methanol dehydrogenation during long-term operation. Then an improved photothermal conversion device was constructed, which could heat Pt_s-CeO_2 to 299°C under one sun irradiation. As a result, the joint system gives rise to an unprecedented ambient sunlight-driven methanol dehydrogenation performance in terms of hydrogen production rate (481.1 mmol g^{-1} h^{-1}), solar-to-H_2 (STH) efficiency (32.9%), and stability (700 hr).

RESULTS AND DISCUSSION

Synthesis of substitutional Pt single atoms in CeO_2 nanosheets

Pt single atoms have been demonstrated to be efficient for methanol dehydrogenation (Wang et al., 2018a). However, oxide-supported Pt single atoms synthesized by the impregnation method generally show the aggregation of Pt species to form Pt nanoparticles when annealing at high temperatures with high loading amounts. Figure S1A shows the atomic-scale scanning transmission electron microscope (STEM) images of 7.1 at% Pt-loaded on CeO_2 nanosheets prepared by impregnation method and annealed at 450°C. It is clear that the Pt species were aggregated as nanoparticles (5 nm, denoted as Pt/CeO_2 450) rather than Pt single atoms. To overcome this problem, we developed a bimetal deposition method with graphene oxides as the template to synthesize substitutional Pt-doped CeO_2 nanosheets in single atomic form (Pt_s-CeO_2) (Gao et al., 2017). As shown in Figure 1A, graphene oxides nanosheets were first dispersed into the aqueous solution containing soluble Pt, Ce precursors. Then, the mixture was freeze-dried to deposit the Pt and Ce metal ions on the surface of graphene oxides (Figure 1A). As Pt and Ce precursors were uniformly deposited on graphene oxides, the sample was annealed at 450°C to remove the graphene oxides and form the Pt-doped CeO_2 nanosheets (denoted as Pt_s-CeO_2) (see Figure S2). X-ray diffraction patterns show only diffraction peaks of CeO_2, and no peak assigned to metallic Pt on Pt_s-CeO_2 (see Figure S3A) (Kong et al., 2020). Energy-dispersive X-ray spectroscope (EDS) shows that the molar content of Pt was 7.4 at% (see Figure S3B). Transmission electron microscope (TEM) images reveal that Pt_s-CeO_2 had nanosheet morphology with a mesoporous structure (Figures 1B and 1C). Figure S4 illustrates 3.1-nm thickness of the nanosheet. STEM-EDS shows that Pt and Ce elements were uniformly distributed over nanosheets (Figure 1D). The atomic-scale STEM image in Figure 1E demonstrates that bright dots were distributed in CeO_2. This suggests that the 7.4 at% of Pt maintained the single atomic form in Pt_s-CeO_2, revealing the capacity of this method for preparing dense Pt single atoms (Figure 1E).

We further characterized the structure difference between Pt_s-CeO_2 and Pt single atoms synthesized by surface impregnation method (Pt_a-CeO_2). Different from the random dispersion of Pt single atoms in Pt_a-CeO_2 (see Figure S1B), the STEM image in Figure 1E clearly shows that Pt atom was located in the lattice position of Ce atom, indicating a substitutional doping mode of Pt in Pt_s-CeO_2. To confirm the coordination structure of Pt in Pt_s-CeO_2, the extended X-ray absorption fine structure (EXAFS) of Pt in Pt_s-CeO_2 was investigated, in comparison with Pt_a-CeO_2 and Pt/CeO_2 450. Fourier transformed EXAFS (FT-EXAFS) of the Pt L_3-edge shows that the peak of Pt in Pt_s-CeO_2 was different from the curve of Pt_a-CeO_2 (Figure 1F and Table S1) and Pt/CeO_2 450, and was similar to the curve of Ce in Pt_s-CeO_2, suggesting the existence of Pt-O

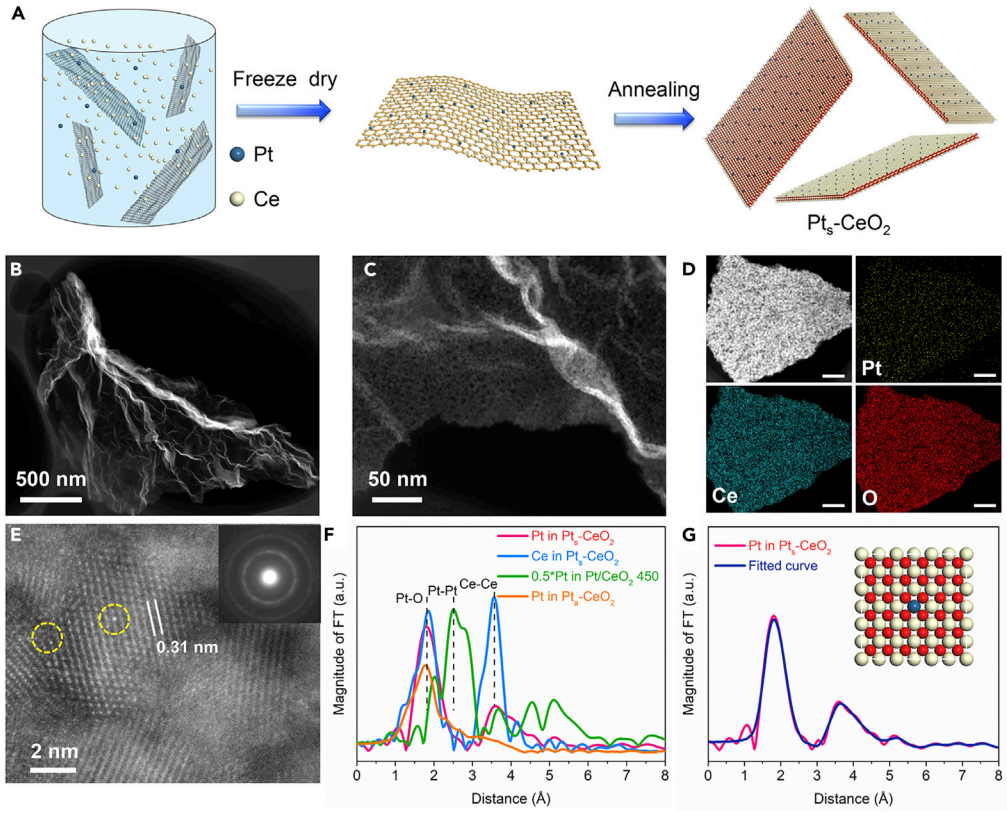

Figure 1. Schematic illustration of synthesis and structure characterization of Pt$_s$-CeO$_2$

(A) Schematic illustration of the synthesis of Pt$_s$-CeO$_2$.

(B–D) (B and C) TEM images and (D) EDS mappings of Pt (yellow), Ce (cyan), and O (red) of Pt$_s$-CeO$_2$.

(E) Atomic scale STEM image of Pt$_s$-CeO$_2$. The inset image in Figure 1E is the SAED pattern.

(F) FT-EXAFS spectra of Pt L_3-edge from Pt$_s$-CeO$_2$, Pt$_a$-CeO$_2$, Pt/CeO$_2$ 450, and Ce K-edge from Pt$_s$-CeO$_2$.

(G) The FT-EXAFS curves of the proposed Pt$_s$-CeO$_2$ structure (blue line) and the measured Pt$_s$-CeO$_2$ (red line). Inset is the proposed model of Pt$_s$-CeO$_2$ architecture.

and Pt-Ce coordination in Pt$_s$-CeO$_2$. The EXAFS simulation (Table S1) shows that the coordination number of Pt-O in Pt$_s$-CeO$_2$ was 7.3, larger than that of Pt in Pt$_a$-CeO$_2$ (4.9). Further, Figure 1G shows that the simulated FT-EXAFS curve of proposed Pt-doped CeO$_2$ model was also well fitted to the curve of Pt$_s$-CeO$_2$. These results confirm that Pt was indeed substitutionally doped in CeO$_2$ nanosheets in single atom form, agreeing well with the STEM result. Therefore, the lattice substitution structure was able to allow the high density of Pt single atoms in Pt$_s$-CeO$_2$ to maintain good thermal stability. The Brunauer-Emmett-Teller specific area of Pt$_s$-CeO$_2$ was 278.5 $m^2\ g^{-1}$ (see Figure S5), ensuring numerous active sites for methanol dehydrogenation. X-ray photoelectron spectroscope (XPS) analysis shows that the Pt $4f_{7/2}$ peak of Pt$_s$-CeO$_2$ was at 72.3 eV (see Figure S6), higher than that of the normal metallic Pt^0 $4f_{7/2}$ state (70.9 eV) (Qiao et al., 2011), indicative of the oxidation state of Pt single atoms in Pt$_s$-CeO$_2$, which might be originated from the substitutional doped structure of single atoms.

Hydrogen production performance from methanol dehydrogenation over Pt$_s$-CeO$_2$

As the catalytic activity of CeO$_2$ nanosheets can be neglected (see Figure S7), we tested the thermocatalytic methanol dehydrogenation ($CH_3OH \rightarrow 2H_2 + CO$) performance of Pt species in Pt$_s$-CeO$_2$ and Pt/CeO$_2$ 450. Compared with Pt/CeO$_2$ 450, Pt$_s$-CeO$_2$ displayed considerably high catalytic performances (Figure 2A). At the temperature of 150°C, the signals of carbon monoxide and hydrogen were detected over Pt$_s$-CeO$_2$ but not over Pt/CeO$_2$ 450. As temperature was increased to 300°C, the hydrogen generation rate was increased to 111.02 mol $g^{-1}_{Pt}\ h^{-1}$ over Pt$_s$-CeO$_2$, equaling to H_2 turnover frequency (TOF) of 21,658 hr^{-1}, which was approximately 11 times that of Pt/CeO$_2$ 450 (10.19 mol $g^{-1}_{Pt}\ h^{-1}$, 1988 h^{-1} of TOF, see Figures 2A and S8). The generation rate of CO was 0.5 times of H_2 at different temperature over Pt$_s$-CeO$_2$ and methanol

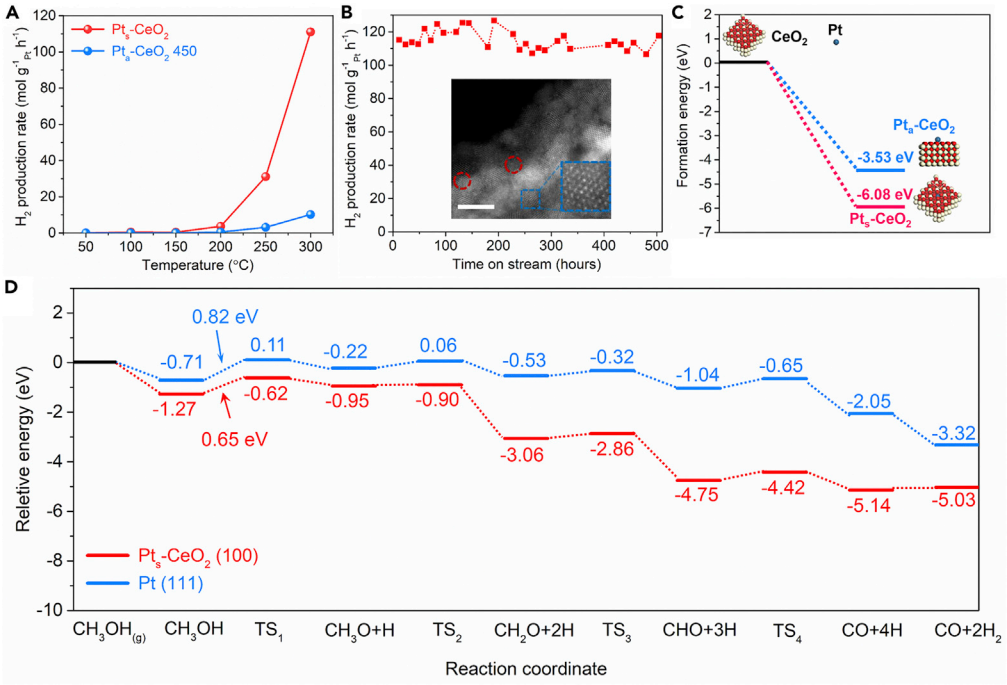

Figure 2. Thermal catalytic activities of Pt$_s$-CeO$_2$ and reaction routes

(A) Hydrogen production rate from methanol in terms of Pt from Pt$_s$-CeO$_2$ and Pt/CeO$_2$ 450 at different temperature.

(B) Methanol dehydrogenation stability of Pt$_s$-CeO$_2$ at 300°C. The inset image in Figure 2B is the atomic scale STEM of Pt$_s$-CeO$_2$ after methanol dehydrogenation.

(C) Structural evolution of Pt and CeO$_2$ in Pt$_a$-CeO$_2$ and Pt$_s$-CeO$_2$ forms.

(D) Energy profiles for CH$_3$OH decomposed as H atoms and CO on Pt$_s$-CeO$_2$ (100) and Pt (111) surfaces. X axis illustrates the intermediates and reaction transition states (TSs); the Y axis illustrates the energy values of each state. The scale bar in (B) is 5 nm.

conversion reached ~6.0% at 300°C (see Figure S9). The methanol dehydrogenation activity of dense Pt single atoms anchored on CeO$_2$ nanosheets (Pt$_a$-CeO$_2$) are reduced sharply at operating temperature of 300°C (see Figure S10A) and the Pt single atoms will be aggregated as Pt nanoparticles after long-term operation (see Figure S10B). Methanol dehydrogenation stability of Pt$_s$-CeO$_2$ was evaluated at 300°C for up to 504 hr. As shown in Figure 2B, the hydrogen generation rate of Pt$_s$-CeO$_2$ was sloshed from 106.58 to 126.74 mol g$^{-1}_{Pt}$ h^{-1}, with no obvious decay trend (Figure 2B). The atom scale STEM (inset image in Figure 2B) and XPS spectrum (see Figure S11) of Pt$_s$-CeO$_2$ after 504 hr reaction showed that the Pt single atoms were not precipitated and the chemical state of Pt remained stable. In addition, TEM image (see Figure S12) shows that Pt$_s$-CeO$_2$ maintained the nanosheet structure after reaction. These results reveal the robust durability and stability of Pt$_s$-CeO$_2$ in methanol dehydrogenation.

The thermal stability and methanol dehydrogenation mechanism of Pt$_s$-CeO$_2$ was examined by density functional theory (DFT) theoretical simulations. The DFT results show that the formation energy of Pt single atoms anchored on CeO$_2$ (Pt$_a$-CeO$_2$ mode) and doped in CeO$_2$ lattice (Pt$_s$-CeO$_2$ mode) is −4.53 and −6.08 eV per Pt atom, respectively (see Figures 2C and S13). This confirms that the Pt$_s$-CeO$_2$ is a more thermodynamically stable structure, which is the reason for robust of Pt$_s$-CeO$_2$ in methanol dehydrogenation. We also calculated the methanol dehydrogenation pathways of Pt$_s$-CeO$_2$ in comparison with metallic Pt nanoparticles (see Figures S14 and S15). As the Pt atoms in Pt$_s$-CeO$_2$ are coordinated to lattice oxygens, the electrons are accumulated to lattice oxygens, which results in the positive theoretical oxidation state (+2.7) of Pt, much higher than that of metallic Pt (+0.42). As shown in Figure 2D, the ability of Pt sites in Pt$_s$-CeO$_2$ for adsorbing methanol (−1.27 eV) is higher than that in Pt nanoparticles (−0.71 eV), revealing the strong methanol adsorption ability of high valence Pt. Detailed decomposition-pathway calculations (Figure 2D) show that the energy barrier for complete CH$_3$OH dissociation to CO*+4H* over Pt$_s$-CeO$_2$ and Pt surface is 0.65 and 0.82 eV, respectively, and the rate-determining step is the decomposition of CH$_3$OH* to CH$_3$O*+H*. This result indicates that the CH$_3$OH decomposition is kinetically more favorable

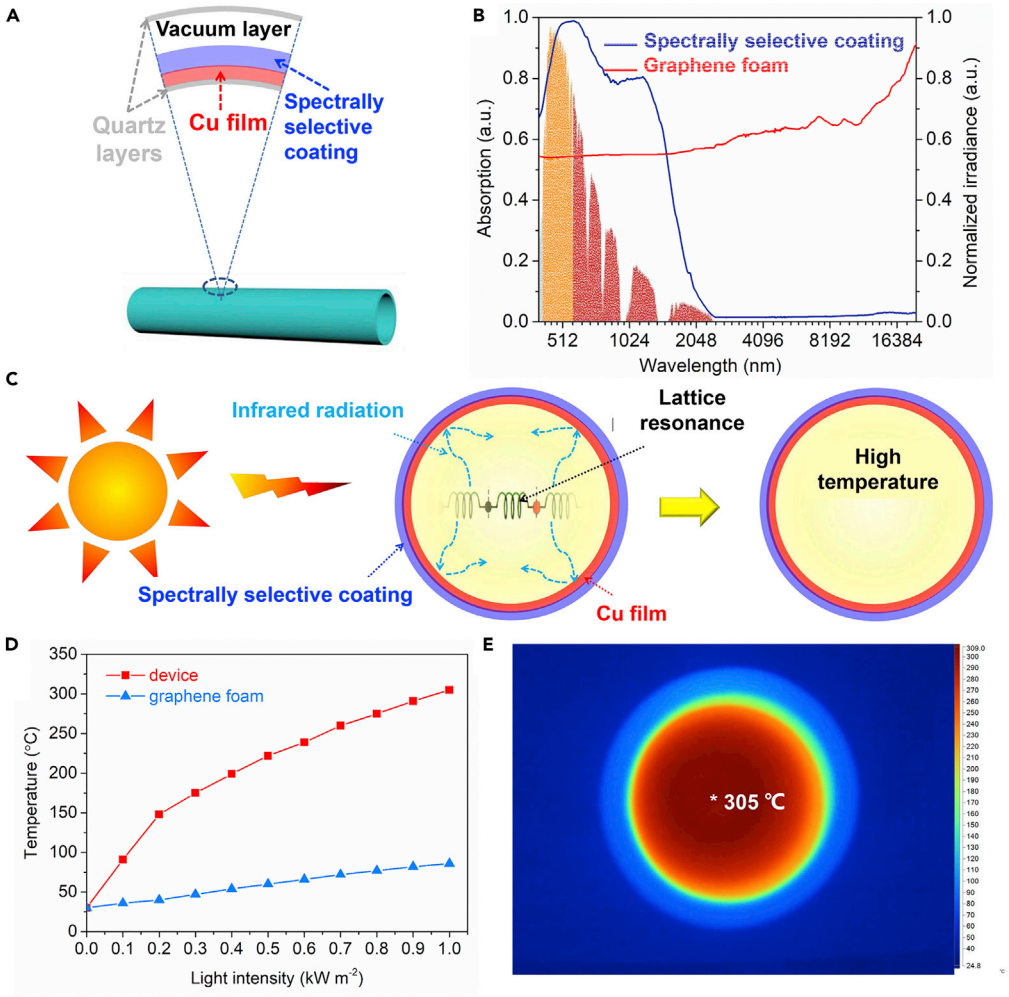

Figure 3. Photothermal system

(A) Schematic of the new photothermal conversion device used for sunlight-driven hydrogen generation form methanol.

(B) Normalized light absorption spectra of the spectrally selective coating and graphene foam ranging from 0.4 to 20 μm.

(C) Sunlight absorption and IR radiation diagram of the new photothermal conversion device shown in Figure 3A.

(D) The temperature of new photothermal conversion device and graphene foam under different sunlight irradiation.

(E) The cross-sectional IR mapping of new photothermal conversion device under one sun irradiation obtained by an IR camera.

on Pt_s-CeO_2. The high adsorption ability and low energy barrier lead to the high activity of Pt_s-CeO_2 for methanol dehydrogenation (Lin et al., 2017; Wang et al., 2019).

Configuration of photothermal conversion device

Ambient sunlight-driven methanol dehydrogenation without additional heat energy input is a sustainable way to produce hydrogen and simultaneously solar energy into chemicals. However, the temperatures of catalysts were generally below 100°C under one sun irradiation (1 kW·m^{-2}); such low temperatures were unable to drive catalytic methanol dehydrogenation. We have recently shown that the temperature of catalysts could amount to ~288°C under one sun irradiation with the assistance of a photothermal conversion device (Li et al., 2019). To obtain a high temperature under one sun irradiation, we further improved the photothermal conversion device. As shown in Figure 3A, the spectrally selective coating ($TiON_x$) was coated on a quartz reaction tube (inner diameter: 7 mm, length: 500 mm) to construct a photothermal conversion device for the purpose of creating high temperature (see Figures S16–S18). Compared with the typical photothermal material graphene foam (see Figure S19) that absorb not only full spectrum of sunlight but also deep (IR) light ranging from 3 to 20 μm (Figure 3B) (Ren et al., 2017; Zhang et al., 2017),

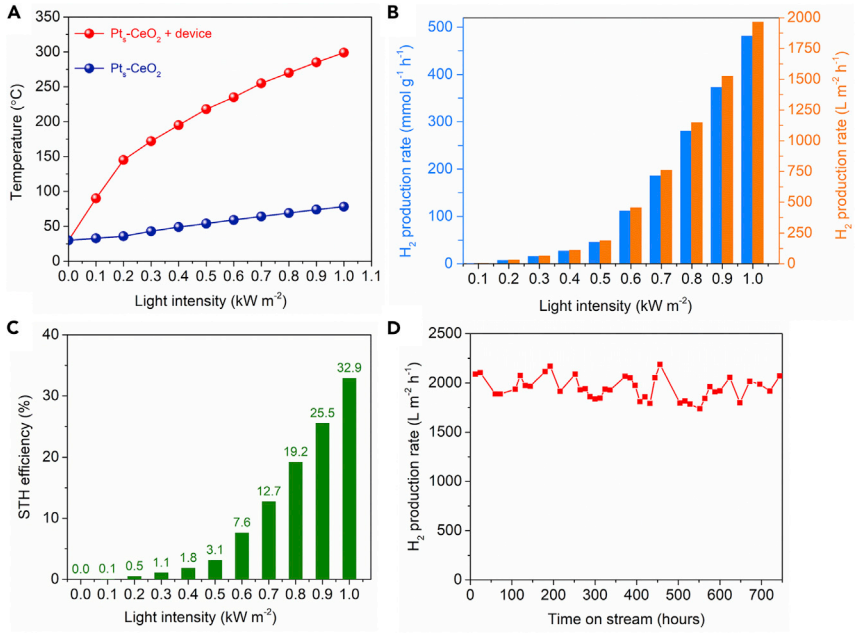

Figure 4. Photothermal catalytic activity of Pt$_s$-CeO$_2$

(A) The temperature of Pt$_s$-CeO$_2$ loaded in the new photothermal conversion device (Pt$_s$-CeO$_2$ + device, red) and in the normal quartz tube (Pt$_s$-CeO$_2$, light blue), respectively, under different sunlight irradiations.

(B and C) Hydrogen generation rate and STH efficiency of Pt$_s$-CeO$_2$ + device under different sunlight irradiations.

(D) Continuous one sun-driven methanol dehydrogenation performance for 744 hr.

spectrally selective coating could strongly absorb sunlight but few IR light (Figure 3B), indicating that it is able to fully absorb sunlight with little IR radiation (Li et al., 2019). Kirchhoff's law illustrates that the IR absorptivity corresponds to the IR radiation capacity of materials (Dao et al., 2015). Therefore, most of heat energy originated from light is dissipated by IR radiation from graphene foam but not from spectrally selective coating (Ghasemi and Ranjbar, 2017). Moreover, a polished Cu film (see Figure S16) was also coated on the tube as shown in Figure 3A, aiming to reflect the IR radiation from the tube and catalysts to block thermal radiation output as shown in Figure 3C (Crawford and Treloar, 2004). In addition to inhibit IR radiation, a vacuum layer (1.7×10^{-3} Pa) was introduced to cover the whole reaction tube to eliminate the heat loss by conduction (Figure 3A). As a result, the inner temperatures of this device (Figure 3D) were consistently much higher than graphene foam under irradiation of sunlight with different intensities (the ambient temperature was 30°C, unless otherwise stated). The maximum inner temperature of this device reached 305°C under 1 sun irradiation (Figure 3E), while only 86°C was obtained from graphene foam by same light irradiation (Figure 3D). In addition, the maximum temperature of this device is around 180°C under 1 sun irradiation without coating Cu film.

Ambient sunlight-driven hydrogen production from methanol

We loaded Pt$_s$-CeO$_2$ in the photothermal conversion device and tested the sunlight-driven methanol dehydrogenation performance. As shown in Figure 4A, the new photothermal conversion device can heat Pt$_s$-CeO$_2$ to 299°C under one sun irradiation (1.0 kW·m^{-2}) (see Figures S20 and S21), while the temperature of Pt$_s$-CeO$_2$ was only 78°C when it was directly irradiated by the same light intensity. The high temperature ensures the operation of methanol dehydrogenation. Hydrogen was even detected under only 0.2 kW·m^{-2} of sunlight irradiation and hydrogen production rate reached 481.1 mmol g^{-1} h^{-1} under 1.0 kW·m^{-2} of sunlight irradiation with methanol conversion (see Figure S22), corresponding to 1964.6 L m^{-2} h^{-1} hydrogen output (Figure 4B), whereas the Pt$_s$-CeO$_2$ cannot decompose the methanol directly irradiated by one sun (see Figure S23). The STH conversion efficiency gradually increased with the intensity of sunlight irradiation and amounted to 32.9% under one sun irradiation (see Figures 4C, S24, and S25). The high STH conversion efficiency obtained at 30°C under 1 sun irradiation is higher than that of other photothermal catalytic systems and was even higher than the value of photoelectric energy conversion efficiency of benchmark Si solar cell (~26%) (Bi et al., 2016). The durability of this photothermal conversion device-supported Pt$_s$-CeO$_2$ system was tested under one solar irradiation. Figure 4D

shows that the hydrogen production rate fluctuated between 1736 L m^{-2} h^{-1} and 2186 L m^{-2} h^{-1} without downward trend for as long as 744 hr, demonstrating excellent long-term stability. The morphology of Pt_s-CeO_2 nanosheets also remained stable after reaction (see Figure S26).

Conclusion

In this work, we developed a bimetal deposition method with graphene oxides as the template to synthesize 7.4 at% of Pt single atoms substitutional doped CeO_2 nanosheets (Pt_s-CeO_2). Pt_s-CeO_2 showed a high hydrogen generation rate of 111.02 mol g^{-1}_{Pt} h^{-1} from methanol dehydrogenation at 300°C, excellent thermal stability and 500 hr level catalytic stability due to the lattice substitution structure of Pt single atoms. Further, a novel photothermal conversion device constructed by Cu film to block IR radiation output, spectrally selective coating to absorb sunlight with little IR radiation and vacuum layer to minimum heat conduction loss, were used to heat Pt_s-CeO_2 to 299°C under one standard solar irradiation at 30°C of ambient temperature. Under 1 sun irradiation, the new photothermal conversion device supported Pt-CeO_2 showed a hydrogen production rate of 476.6 mmol g^{-1} h^{-1} or 1946 L m^{-2} h^{-1} from methanol with a month level stability, corresponding to STH efficiency of 32.9%. Our strategy of combining efficient single atom catalysts and photothermal conversion device demonstrates a potential efficient ambient sunlight-driven hydrogen generation strategy from methanol without additional energy input and may be applicable to other catalytic reactions to realize efficient solar to chemical energy conversion.

Limitations of the study

Here, we carried out experiments of sunlight-driven photothermal methanol dehydrogenation for syngas production with 32.9% STH conversion efficiency in our laboratory, where the produced toxic CO can be well handled. Due to the concerns about producing large amounts of toxic CO, it is unfeasible for us to perform the outdoor experiments using the current photothermal device. However, considering that the production of syngas is already very mature in industry, we believe that the outdoor experiments could be viable by improving the experimental equipment.

Resource availability

Lead contact

Further information and requests for resources and materials should be directed to and will be fulfilled by the lead contact, Jinhua Ye (Jinhua.YE@nims.go.jp).

Materials availability

All chemicals were obtained from commercial resources and used as received.

Data and code availability

There is no data set or code associated with this work.

METHODS

All methods can be found in the accompanying Transparent methods supplemental file.

SUPPLEMENTAL INFORMATION

Supplemental information can be found online at https://doi.org/10.1016/j.isci.2021.102056.

ACKNOWLEDGMENTS

This work is supported by the National Natural Science Foundation of China (Grant Nos. 51702078 and 21633004), Hebei Provincial Department of Education Foundation (Grant No. BJ2019016), Outstanding Doctoral Cultivation Project of Hebei University (YB201502), JSPS KAKENHI (No. JP18H02065), the Photo-excitonix Project at Hokkaido University, the World Premier International Research Center Initiative (WPI Initiative) on Materials Nanoarchitectonics (MANA), MEXT (Japan). Thanks for the TEM technical supports provided by the Microanalysis Center, College of Physics Science and Technology, Hebei University. We acknowledge the Shanghai Synchrotron Radiation Facility for conducting the EXAFS experiment (BL14W1).

AUTHOR CONTRIBUTIONS

Conceptualization, Y. G. Li, H. Song and J. H. Ye.; Resources, Y. G. Li, X. H. Bai and D. C. Yuan Investigation, X. H. Bai; Formal Analysis, J. M. Lu., Y. F. Lu and X. Y. San; Writing – Original Draft Y. G. Li and H.S.; Writing – Review & Editing Y. G. Li, H. S., F. Wang and G. S. Fu. Supervision, J. H. Ye.

DECLARATION OF INTERESTS

The authors declare that they have no known competing financial interests or personal relationships that could have appeared to influence the work reported in this paper.

Received: November 30, 2020
Revised: January 4, 2021
Accepted: January 7, 2021
Published: February 19, 2021

REFERENCES

Asthana, S., Samanta, C., Voolapalli, R.K., and Saha, B. (2017). Direct conversion of syngas to DME: synthesis of new Cu-based hybrid catalysts using Fehling's solution, elimination of the calcination step. J. Mater. Chem. A *5*, 2649–2663.

Bae, K., Kang, G., Cho, S.K., Park, W., Kim, K., and Padilla, W.J. (2015). Flexible thin-film black gold membranes with ultrabroadband plasmonic nanofocusing for efficient solar vapour generation. Nat. Commun. *6*, 10103.

Bi, D., Yi, C., Luo, J., Décoppet, J.-D., Zhang, F., Zakeeruddin, Shaik M., Li, X., Hagfeldt, A., and Grätzel, M. (2016). Polymer-templated nucleation and crystal growth of perovskite films for solar cells with efficiency greater than 21%. Nat. Energy *1*, 16142.

Brown, J.C., and Gulari, E. (2004). Hydrogen production from methanol decomposition over Pt/Al2O3 and ceria promoted Pt/Al2O3 catalysts. Catal. Commun. *5*, 431–436.

Chai, Z., Zeng, T.-T., Li, Q., Lu, L.-Q., Xiao, W.-J., and Xu, D. (2016). Efficient visible light-driven splitting of alcohols into hydrogen and corresponding carbonyl compounds over a Ni-modified CdS photocatalyst. J. Am. Chem. Soc. *138*, 10128–10131.

Chen, X., Shen, S., Guo, L., and Mao, S.S. (2010). Semiconductor-based photocatalytic hydrogen generation. Chem. Rev. *110*, 6503–6570.

Chen, Y., Ji, S., Wang, Y., Dong, J., Chen, W., Li, Z., Shen, R., Zheng, L., Zhuang, Z., Wang, D., et al. (2017). Isolated single iron atoms anchored on N-doped porous carbon as an efficient electrocatalyst for the oxygen reduction reaction. Angew. Chem. Int. Ed. *56*, 6937–6941.

Crawford, R.H., and Treloar, G.J. (2004). Net energy analysis of solar and conventional domestic hot water systems in Melbourne, Australia. Solar Energy *76*, 159–163.

Dao, T.D., Chen, K., Ishii, S., Ohi, A., Nabatame, T., Kitajima, M., and Nagao, T. (2015). Infrared perfect absorbers fabricated by colloidal mask etching of Al–Al_2O_3–Al trilayers. ACS Photon. *2*, 964–970.

Dry, M.E. (2002). The Fischer–Tropsch process: 1950–2000. Catal. Today *71*, 227–241.

Gao, L., Li, Y., Xiao, M., Wang, S., Fu, G., and Wang, L. (2017). Synthesizing new types of ultrathin 2D metal oxide nanosheets via half-successive ion layer adsorption and reaction. 2D Mater. *4*, 025031.

Ghasemi, S.E., and Ranjbar, A.A. (2017). Effect of using nanofluids on efficiency of parabolic trough collectors in solar thermal electric power plants. Inter. J. Hydro. Energy *42*, 21626–21634.

Govindarajan, N., Sinha, V., Trincado, M., Grützmacher, H., Meijer, E.J., and de Bruin, B. (2020). An in-depth mechanistic study of Ru-catalysed aqueous methanol dehydrogenation and prospects for future catalyst design. ChemCatChem *12*, 2610–2621.

Huang, H., Jin, Y., Chai, Z., Gu, X., Liang, Y., Li, Q., Liu, H., Jiang, H., and Xu, D. (2019). Surface charge-induced activation of Ni-loaded CdS for efficient and robust photocatalytic dehydrogenation of methanol. Appl. Catal. B Environ. *257*, 117869.

Huber, G.W., Iborra, S., and Corma, A. (2006). Synthesis of transportation fuels from biomass: chemistry, catalysts, and engineering. Chem. Rev. *106*, 4044–4098.

Khodakov, A.Y., Chu, W., and Fongarland, P. (2007). Advances in the development of novel cobalt Fischer–Tropsch catalysts for synthesis of long-chain hydrocarbons and clean fuels. Chem. Rev. *107*, 1692–1744.

Kong, J., Xiang, Z., Li, G., and An, T. (2020). Introduce oxygen vacancies into CeO_2 catalyst for enhanced coke resistance during photothermocatalytic oxidation of typical VOCs. Appl. Catal. B Environ. *269*, 118755.

Kudo, A., and Miseki, Y. (2009). Heterogeneous photocatalyst materials for water splitting. Chem. Soc. Rev. *38*, 253–278.

Li, Y., Hao, J., Song, H., Zhang, F., Bai, X., Meng, X., Zhang, H., Wang, S., Hu, Y., and Ye, J. (2019). Selective light absorber-assisted single nickel atom catalysts for ambient sunlight-driven CO_2 methanation. Nat. Commun. *10*, 2359.

Lin, L., Zhou, W., Gao, R., Yao, S., Zhang, X., Xu, W., Zheng, S., Jiang, Z., Yu, Q., Li, Y.-W., et al. (2017). Low-temperature hydrogen production from water and methanol using Pt/α-MoC catalysts. Nature *544*, 80–83.

Liu, Y., Yang, S., Yin, S.-N., Feng, L., Zang, Y., and Xue, H. (2018). In situ construction of fibrous AgNPs/g-C_3N_4 aerogel toward light-driven COx-free methanol dehydrogenation at room temperature. Chem. Eng. J. *334*, 2401–2407.

Liu, Z., Yin, Z., Cox, C., Bosman, M., Qian, X., Li, N., Zhao, H., Du, Y., Li, J., and Nocera, D.G. (2016). Room temperature stable COx-free H_2 production from methanol with magnesium oxide nanophotocatalysts. Sci. Adv. *2*, e1501425.

Marbán, G., López, A., López, I., and Valdés-Solís, T. (2010). A highly active, selective and stable copper/cobalt-structured nanocatalyst for methanol decomposition. Appl. Catal. B Environ. *99*, 257–264.

Mostafa, S., Croy, J.R., Heinrich, H., and Cuenya, B.R. (2009). Catalytic decomposition of alcohols over size-selected Pt nanoparticles supported on ZrO_2: a study of activity, selectivity, and stability. Appl. Catal. A *366*, 353–362.

O'Brien, P.G., Ghuman, K.K., Jelle, A.A., Sandhel, A., Wood, T.E., Loh, J.Y.Y., Jia, J., Perovic, D., Singh, C.V., Kherani, N.P., et al. (2018). Enhanced photothermal reduction of gaseous CO_2 over silicon photonic crystal supported ruthenium at ambient temperature. Energy Environ. Sci. *11*, 3443–3451.

Oara Neumann, A.S.U., Day, J., Lal, S., Peter, N., and Halas, N.J. (2013). Solar vapor generation enabled by nanoparticles. ACS Nano *7*, 42–49.

Palo, D.R., Dagle, R.A., and Holladay, J.D. (2007). Methanol steam reforming for hydrogen production. Chem. Rev. *107*, 3992–4021.

Pang, Y., Uddin, M.N., Chen, W., Javaid, S., Barker, E., Li, Y., Suvorova, A., Saunders, M., Yin, Z., and Jia, G. (2019). Colloidal single-layer photocatalysts for methanol-storable solar H_2 fuel. Adv. Mater. *31*, 1905540.

Paulino, R.F.S., Essiptchouk, A.M., and Silveira, J.L. (2020). The use of syngas from biomedical waste plasma gasification systems for electricity production in internal combustion: Thermodynamic and economic issues. Energy *199*, 117419.

Qiao, B., Wang, A., Yang, X., Allard, L.F., Jiang, Z., Cui, Y., Liu, J., Li, J., and Zhang, T. (2011). Single-atom catalysis of CO oxidation using Pt1/FeOx. Nat. Chem. *3*, 634.

Ren, H., Tang, M., Guan, B., Wang, K., Yang, J., Wang, F., Wang, M., Shan, J., Chen, Z., Wei, D., et al. (2017). Hierarchical graphene foam for efficient omnidirectional solar–thermal energy conversion. Adv. Mater. *29*, 1702590.

Sordakis, K., Tang, C., Vogt, L.K., Junge, H., Dyson, P.J., Beller, M., and Laurenczy, G. (2018). Homogeneous catalysis for sustainable hydrogen storage in formic acid and alcohols. Chem. Rev. *118*, 372–433.

Wang, A., Li, J., and Zhang, T. (2018a). Heterogeneous single-atom catalysis. Nat. Rev. Chem. *2*, 65–81.

Wang, C., Zhang, J., Qin, G., Wang, L., Zuidema, E., Yang, Q., Dang, S., Yang, C., Xiao, J., Meng, X., et al. (2020). Direct conversion of syngas to ethanol within zeolite crystals. Chem *6*, 646–657.

Wang, K., Wei, Z., Ohtani, B., and Kowalska, E. (2018b). Interparticle electron transfer in methanol dehydrogenation on platinum-loaded titania particles prepared from P25. Catal. Today *303*, 327–333.

Wang, L., Ghoussoub, M., Wang, H., Shao, Y., Sun, W., Tountas, A.A., Wood, T.E., Li, H., Loh, J.Y.Y., Dong, Y., et al. (2018c). Photocatalytic hydrogenation of carbon dioxide with high selectivity to methanol at atmospheric pressure. Joule *2*, 1369–1381.

Wang, Q., Chen, L., Liu, Z., Tsumori, N., Kitta, M., and Xu, Q. (2019). Phosphate-mediated immobilization of high-performance AuPd nanoparticles for dehydrogenation of formic acid at room temperature. Adv. Fun. Mater. *29*, 1903341.

Wang, X., Chen, W., Zhang, L., Yao, T., Liu, W., Lin, Y., Ju, H., Dong, J., Zheng, L., Yan, W., et al. (2017). Uncoordinated amine groups of metal-organic frameworks to anchor single Ru sites as chemoselective catalysts toward the hydrogenation of quinoline. J. Am. Chem. Soc. *139*, 9419–9422.

Wei, H., Liu, X., Wang, A., Zhang, L., Qiao, B., Yang, X., Huang, Y., Miao, S., Liu, J., and Zhang, T. (2014). FeOx-supported platinum single-atom and pseudo-single-atom catalysts for chemoselective hydrogenation of functionalized nitroarenes. Nat. Commun. *5*, 5634.

Xiao, J.-D., and Jiang, H.-L. (2019). Metal–organic frameworks for photocatalysis and photothermal catalysis. Acc. Chem. Res. *52*, 356–366.

Xu, N., Hu, X., Xu, W., Li, X., Zhou, L., Zhu, S., and Zhu, J. (2017). Mushrooms as efficient solar steam-generation devices. Adv. Mater. *29*, 06762.

Yang, H.B., Hung, S.-F., Liu, S., Yuan, K., Miao, S., Zhang, L., Huang, X., Wang, H.-Y., Cai, W., Chen, R., et al. (2018). Atomically dispersed Ni(i) as the active site for electrochemical CO_2 reduction. Nat. Energy *3*, 140–147.

Zeng, Y., Wang, K., Yao, J., and Wang, H. (2014). Hollow carbon beads for significant water evaporation enhancement. Chem. Eng. Sci. *116*, 704–709.

Zhang, P., Li, J., Lv, L., Zhao, Y., and Qu, L. (2017). Vertically aligned graphene sheets membrane for highly efficient solar thermal generation of clean water. ACS Nano *11*, 5087–5093.

Zhao, C., Dai, X., Yao, T., Chen, W., Wang, X., Wang, J., Yang, J., Wei, S., Wu, Y., and Li, Y. (2017). Ionic exchange of metal-organic frameworks to access single nickel sites for efficient electroreduction of CO_2. J. Am. Chem. Soc. *139*, 8078–8081.

iScience, Volume *24*

Supplemental Information

Ambient sunlight-driven photothermal methanol dehydrogenation for syngas production with 32.9 % solar-to-hydrogen conversion efficiency

Xianhua Bai, Dachao Yuan, Yaguang Li, Hui Song, Yangfan Lu, Xingyuan San, Jianmin Lu, Guangsheng Fu, Shufang Wang, and Jinhua Ye

Transparent Methods

Materials

Commercial cerium nitrate hydrate ($Ce(NO_3)_2 \cdot 6H_2O$), chloroplatinic acid hydrate ($H_2PtCl_6 \cdot 6H_2O$) were bought from Sinopharm Co., Ltd. Graphene oxides (GO) were synthesized by hummers method (Chen et al., 2013). Xicheng Special Gas Co., Ltd provided the liquid nitrogen. The chemicals were all used without any further treatment. Hebei scientist research experimental and equipment trade Co., Ltd provided spectrally selective coating and synthesized the new photothermal device shown in Figure 3A and Figure S16-18. The emissivity of this device is 0.03.

Synthesis of Pt_s-CeO_2

200 mg GO was added into 200 mL water and was stirred for 1 h. Then, 100 mg $Ce(NO_3)_2 \cdot 6H_2O$ and 9 mg $H_2PtCl_6 \cdot 6H_2O$ were added into the above solution. After stirring for 15 mins, the solution was added into the liquid nitrogen in 1 minute and freeze-dried for 5 days by freeze dryer (FD-1A-50). The Pt_s-CeO_2 was obtained by annealing the above sample at 450 °C in air for 12 hours with heating rate of 2 °C min^{-1}.

Synthesis of CeO_2 nanosheets, Pt_a-CeO_2 and Pt/CeO_2

The synthesis of CeO_2 nanosheets was similar to the procedures of Pt_s-CeO_2 except that the Pt precursor was not added.

For the synthesis of Pt_a-CeO_2, 100 mg CeO_2 nanosheets and 23 mg $H_2PtCl_6 \cdot 6H_2O$ were mixed with 5 mL of water for 10 minutes to form a uniform mud. Then the mud was freeze as ice and freeze-dried for 2 days to remove the water. Finally, the dried sample was annealed at 200 and 450 °C in air for 12 hours with heating rate of 2 °C min^{-1} to form the Pt_a-CeO_2, Pt/CeO_2 450, respectively.

Synthesis of graphene foam.

20 mL aqueous solution containing 100 mg GO was stirred for 1 h, and then was frozen by refrigerator. The sample was freeze-dried for 5 days. Then the dried sample was reduced by 1 mL of hydrazine hydrate at 100 °C for 12 hours to obtain the graphene foam.

Characterizations.

XRD was characterized by a Bruker D8 Advance diffractometer with a Cu Ka radiation (λ= 1.541 Å) at 20 kV. ARM 200F and JEOL F200+ were applied for the TEM, STEM and elemental mapping. The optical properties were investigated by a Shimadzu UV3600 UV–Vis spectrophotometer and a FTIR spectrometer (Bruker, VERTEX 70 FT-IR). Fluke Ti300 IR camera (America) was used to take IR picture. Platinum resistance thermometer (M363886) was used for detecting the data of temperatures. Thermo ESCALAB-250 spectrometer with a monochromatic Al Kα radiation source (1486.6 eV) was used to detect valence state of materials. Micromeritics Tristar 3020 system was used to test the specific surface area of catalysts. The Pt L_3-edge, Ce K-edge extended X-ray absorption fine structure (EXAFS) data were tested by the BL14W1 beamline of Shanghai Synchrotron Radiation Facility (SSRF). Athena software was used to calibrate the energy scale, correct the background of signals, normalize intensity of signals and fourier transformed the data in k-space. Atomic force microscopy (AFM, Cypher ES) was used to detect the thickness of samples.

Thermal catalytic test of hydrogen production from methanol

The thermal catalytic activity of hydrogen generation from methano was tested by the fixed-bed reactor (XM190708-007, DALIAN ZHONGJIARUILIN LIQUID TECHNOLOGY CO., LTD) in continuous flow reactor. Typically, 2 mg catalyst was placed in a quartz flow reactor. 0.1 mL min^{-1} of methanol controlled by the peristaltic pump with 100 mL min^{-1} Ar as carrier was used as the feed gas for methanol dehydrogenation. The outlet gases were tested by gas chromatograph (GC, Agilent 7890A) equipped with FID and TCD detector (Column: TDX-01, 2 m; Column temperature: 150 °C, TCD detection temperature: 230 °C, FID detection temperature: 270 °C). The turnover frequency (TOF) was calculated according to the following equation: TOF = (number of mole of H_2)/(number of moles of Pt×time).

Sunlight-driven hydrogen production from methanol

The laboratory light source used for photothermal test was a customized product (HP-2-4000, provided by Hebei scientist research experimental and equipment trade Co., Ltd). The light spectrum was similar to AM 1.5 G as shown in Figure S20.

40 mg prepared catalysts were loaded in a quartz tube or the photothermal conversion device (irradiation area 2.4 cm^2, Figure S24) irradiated by HP-2-4000. The irradiation intensity was tuned from 0.1 kW m^{-2} to 1 kW m^{-2}. The mixture of 150 mL min^{-1} Ar and 0.15 mL min^{-1} methanol was introduced into the reactor. The light source HP-2-4000 was used to full irradiate the reactor and the ambient temperature was constant at 30 °C. T The outlet gases were tested by gas chromatograph (GC, Agilent 7890A) equipped with FID and TCD detector (Column: TDX-01, 2 m; Column temperature: 150 °C, TCD detection temperature: 230 °C, FID detection temperature: 270 °C).

1. The H_2 generation rate for per gram of catalyst (δ, mmol g^{-1}_{cat} h^{-1}) was calculated as follows:

$$\delta \text{ (mmol } g^{-1}_{cat} h^{-1}) = (1000*K*L*60/24.5)/G \quad (1)$$

K is the H_2 concentration detected by GC, L is the was flow rate (0.15 L min^{-1}), G was the weight of catalysts (0.04 g).

2. The plate form H_2 generation rate (η, L m^{-2} h^{-1}) was calculated as follows:

$$\eta \text{ (L } m^{-2} h^{-1}) = K*L*60/S \quad (2)$$

K is the H_2 concentration detected by GC, L was the gas flow rate (0.15 L min^{-1}), S was the irradiated area of catalysts (0.00024 m^{-2}).

3. The STH efficiency of hydrogen generation from methanol was calculated as follows:

$$\text{STH (\%)} = \text{Output energy as } H_2 \text{ / Energy of incident sunlight} \times 100\% = (R(H_2) \times \Delta G) / (I \times S) \times 100\% = ((K \times L /24.5) \times \Delta G)/(I \times S) \quad (3)$$

ΔG is the reaction Gibbs energy of methanol dehydrogenation (1/2 CH_3OH (l) → H_2 (g)+ 1/2 CO (g), ΔG=14.77 kJ mol^{-1}); $R(H_2)$ is the H_2 production rate; I is the light intensity (kW m^{-2}); S is the irradiated area of catalysts (0.00024 m^{-2}); K is the H_2 concentration detected by GC (%); L is the gas flow rate (0.0025 L s^{-1}); 24.5 L mol^{-1} is the molar volume under ambient conditions. According to Figure S25 A and C, under 1.0 kW·m^{-2} of sunlight irradiation, K=70804/13511=5.24%. Therefore, STH = ((5.24% × 0.0025/24.5) × 14.77)/(1 × 0.00024)= 32.9%.

First principle calculations

The Vienna Ab Initio Package (VASP) was used to conduct all the DFT calculations within the generalized gradient approximation (GGA) using the PBE formulation (Perdew et al., 1996). The projected augmented wave (PAW) potentials (Blöchl, 1994; Kresse and Joubert, 1999) were chosen to describe the ionic cores and take valence electrons into account using a plane wave basis set with a kinetic energy cutoff of 400 eV. Partial occupancies of the Kohn−Sham orbitals were allowed using the Gaussian smearing method and a width of 0.05 eV. The electronic energy was considered self-consistent when the energy change was smaller than 10^{-7} eV. A geometry optimization was considered convergent when the energy change was smaller than 10^{-6} eV. Grimme's DFT-D3 methodology (Grimme et al., 2010) was used to describe the dispersion interactions among all the atoms in the bulk unit cells and surface models of interest. The transition states were calculated by the climbing image nudged elastic band method (CI-NEB) (Henkelman et al., 2000). The adsorption energy (δ) shown in Figure 2d (The energy of $CH_3OH_{(g)}$, CH_3OH, CH_3O+H, CH_2O+2H, CHO+3H, CO+4H) was calculated by the equation of

$$\delta = E_{c/slab} - (E_{slab} + E_c) \quad (4)$$

In this equation, $E_{c/slab}$ and E_{slab} was the total energy of slab with and without alien adsorbed species in equilibrium geometry, respectively. E_c was the total energy of CH_3OH in gas phase. Consequently, the more negative value of adsorption energy means the stronger of adsorption.

The reaction barrier energy (E_b) was calculated by

$$E_b = E_{c/slab} - E_{TS} \quad (5)$$

E_{TS} was the energy of the TS_1, TS_2, TS_3, TS_4. And the $E_{c/slab}$ only subtracts the followed E_{TS} shown in Figure 2d. The equilibrium lattice constant of Pt cell was 3.918 Å and the bond of Pt-Pt is in the length of 2.768 Å. The lattice constant of cubic CeO_2 was calculated to be 5.418 Å. The cleave surface models were CeO_2 (100) and Pt (111). Totally, the CeO_2 (100) surface had 72 Ce and 144 O, where 54 Ce and 108 O atoms were fixed; the Pt (111) has 108 Pt atoms, and 72 of them were fixed; the Pt-CeO_2 (100) had 1 Pt, 71 Ce and 144 O atoms, of which 54 Ce and 108 O atoms were fixed, and the pt coverage was 1/18.

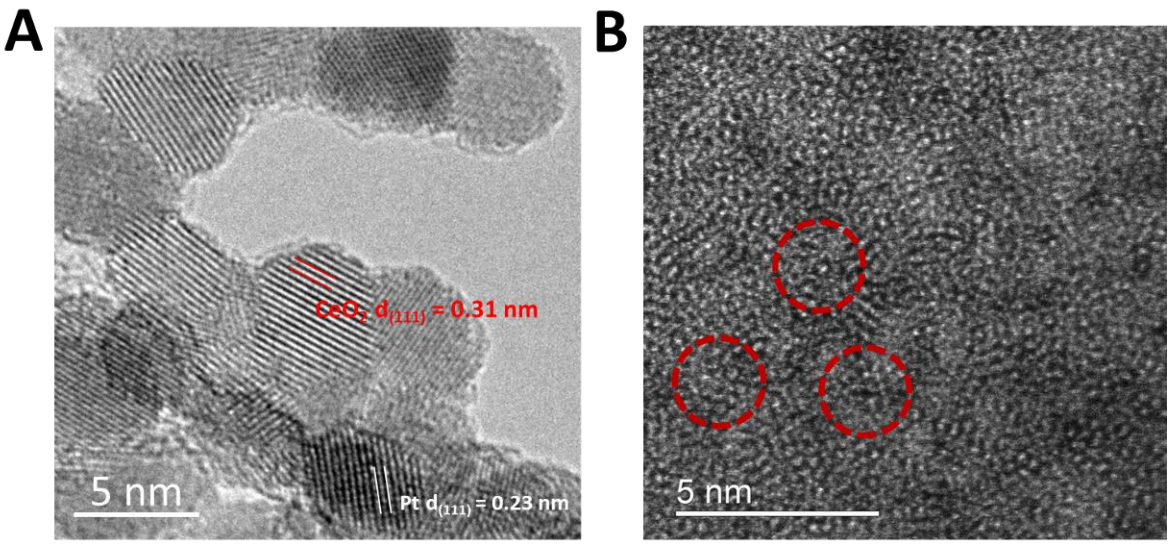

Figure S1. Related to Figure 1. (A) Atomic scale STEM image of Pt/CeO_2 450. (B) Atomic scale STEM image of Pt_a-CeO_2.

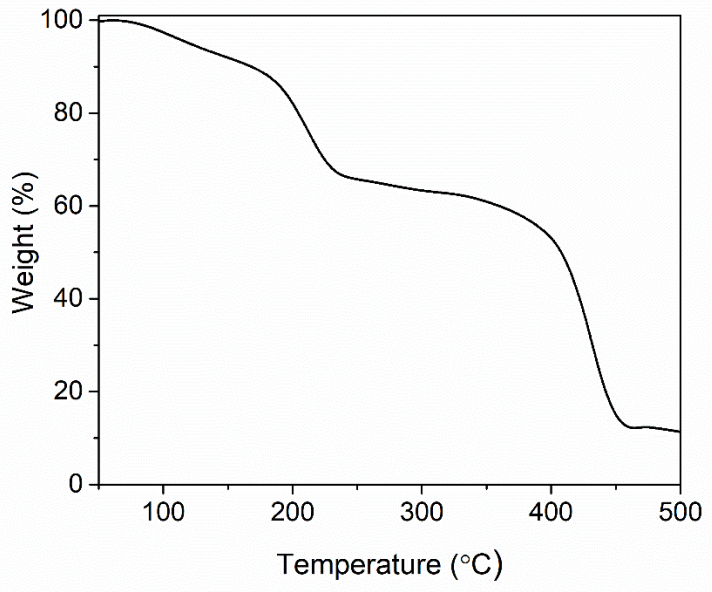

Figure S2. Related to Figure 1. TGA of Pt-CeO_2 precursor. The weight loss above 200 ˚C is attributed to burning of GO.

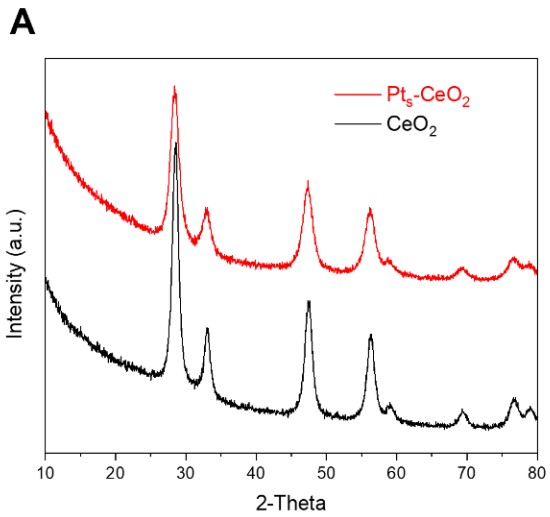

B

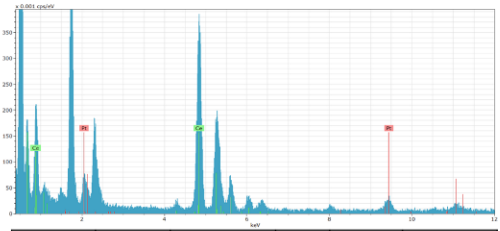

Element	Series	Net counts	Wt.%	At.%	Error wt.%
Pt	L	1550	10.0	7.4	3.3
Ce	L	18728	90.0	92.6	27.2
		Sum:	100	100	

Figure S3. Related to Figure 1. (A) XRD patterns of Pt_s-CeO_2 and CeO_2 nanosheets. (B) EDS and Pt, Ce ratio in Pt_s-CeO_2.

The phase card of Pt_s-CeO_2 and CeO_2 nanosheets is PDF# 43-1002.

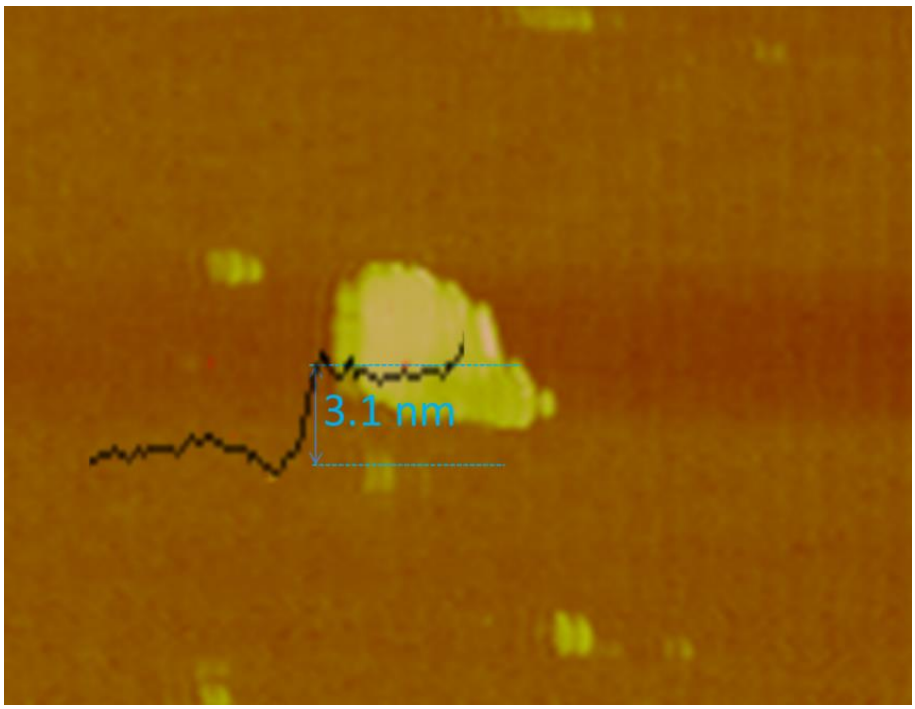

Figure S4. Related to Figure 1. The AFM image of Pt_s-CeO_2.

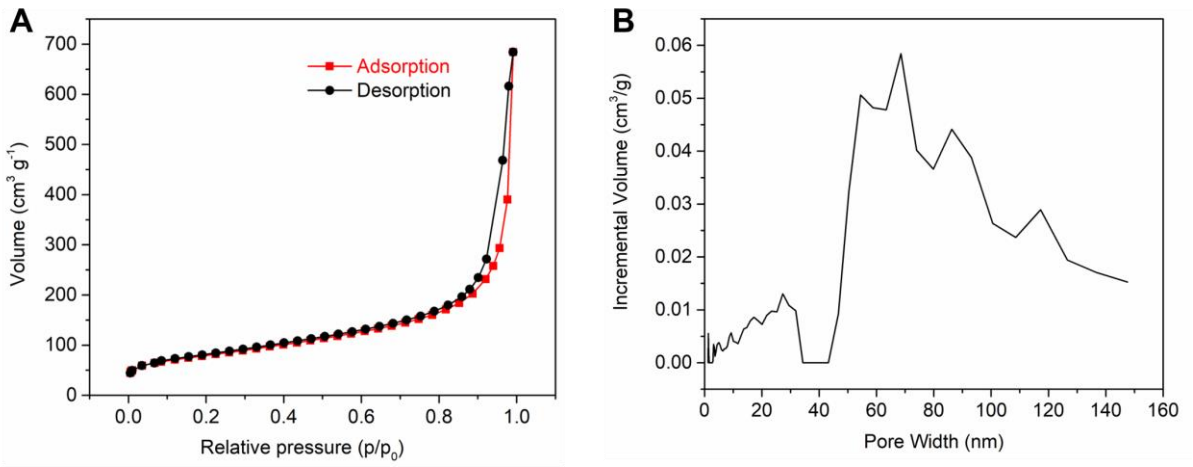

Figure S5. Related to Figure 1. (A) N_2 adsorption-desorption isotherm of Pt_s-CeO_2. (B) Pore size distribution of Pt_s-CeO_2. The pore size distribution was obtained using adsorption branch via N_2- DFT model.

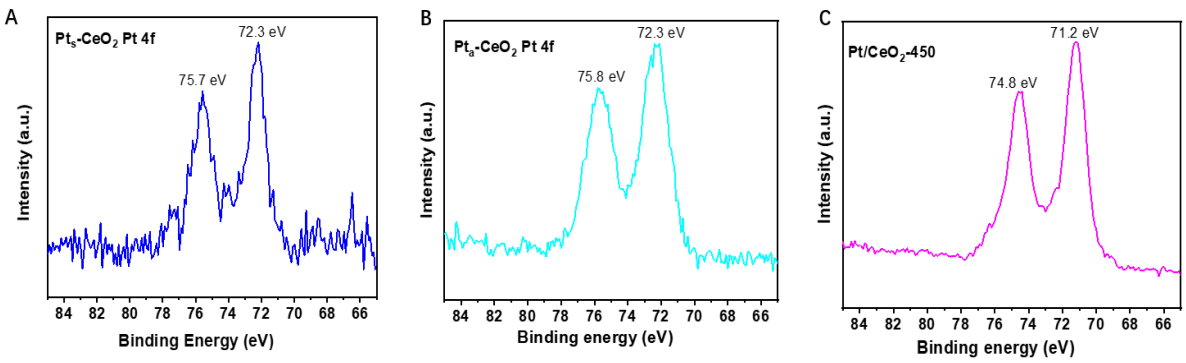

Figure S6. Related to Figure 1. The XPS spectra of Pt 4f in (A) Pt_s-CeO_2, (B) Pt_a-CeO_2, (C) Pt/CeO_2 450. As shown in Figure S6, the Pt $4f_{7/2}$ XPS peaks of Pt_s-CeO_2 and Pt_a-CeO_2 is at 72.3 eV and 72.3eV, respectively, higher than that of Pt/CeO_2-450 (71.2 eV).

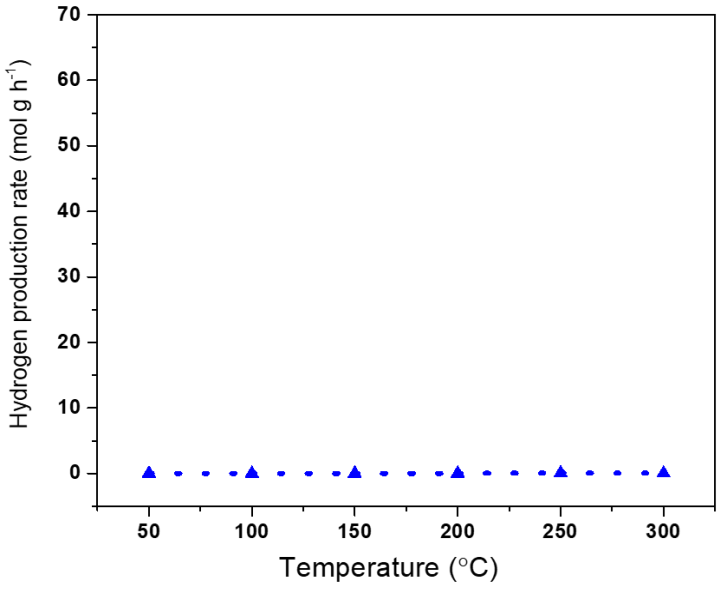

Figure S7. Related to Figure 2. Hydrogen production rate from methanol in terms of CeO_2 nanosheets at different temperature.

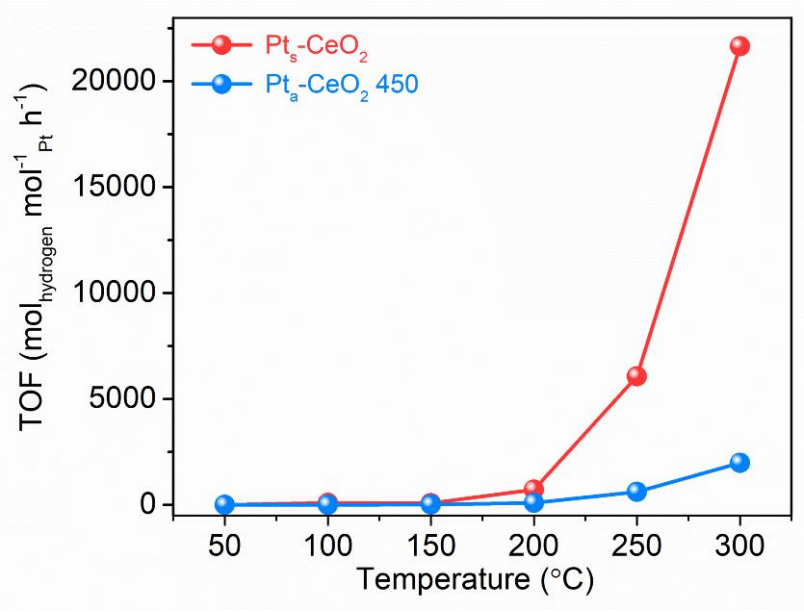

Figure S8. Related to Figure 2. Turnover frequency (TOF) of H_2 from methanol in terms of H_2 production per Pt site of Pt_s-CeO_2 and Pt-CeO_2 450 at different temperatures.

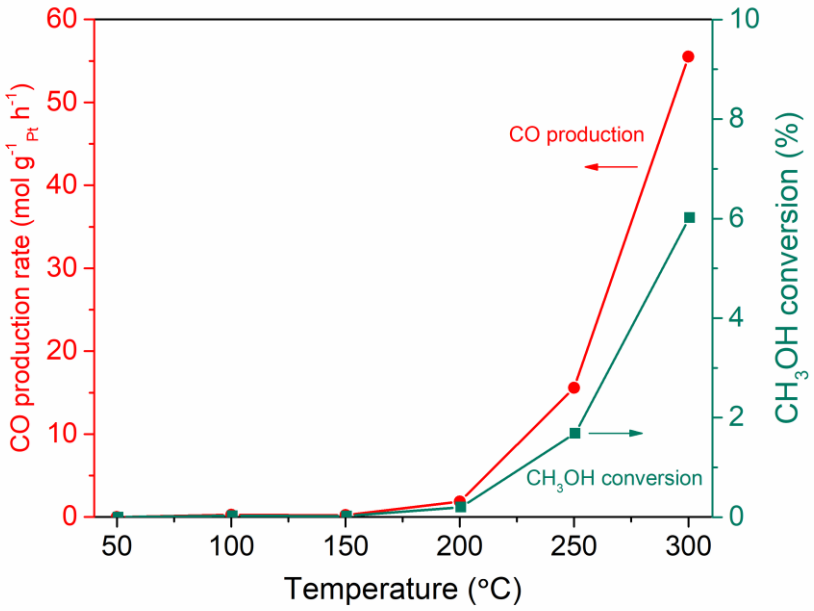

Figure S9. Related to Figure 2. CO production rate and methanol conversion over Pt_s-CeO_2 at different temperature.

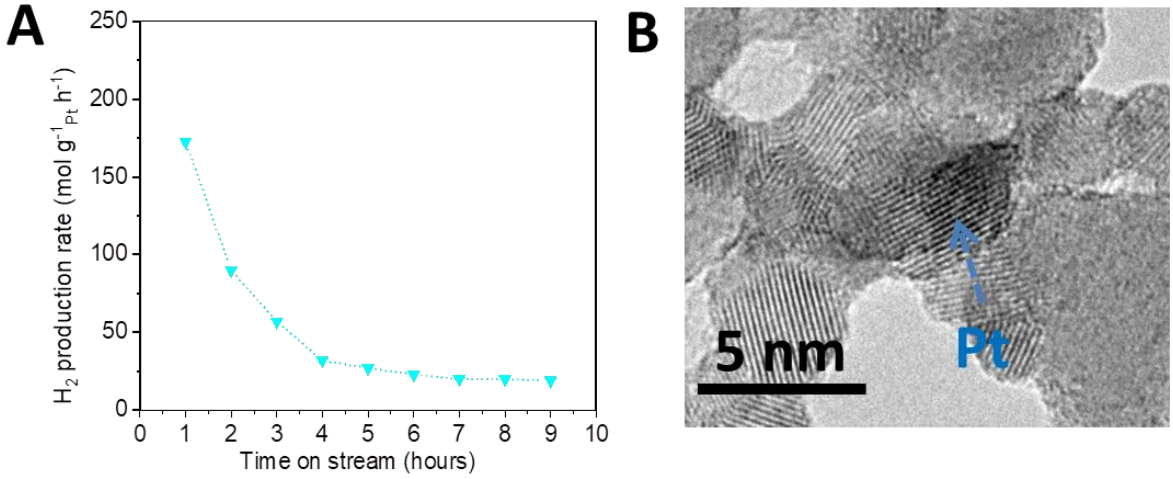

Figure S10. Related to Figure 2. (A) Methanol dehydrogenation stability of Pt_a-CeO_2 at 300 °C. (B) The HRTEM images of Pt_a-CeO_2 after 24 hours of thermal methanol dehydrogenation at 300 °C. As shown in Figure S10A, Pt_a-CeO_2 showed unstable performance and the Pt species aggregated into nanoparticles (Figure S10B), indicating the instability of Pt_a-CeO_2 in thermal methanol dehydrogenation.

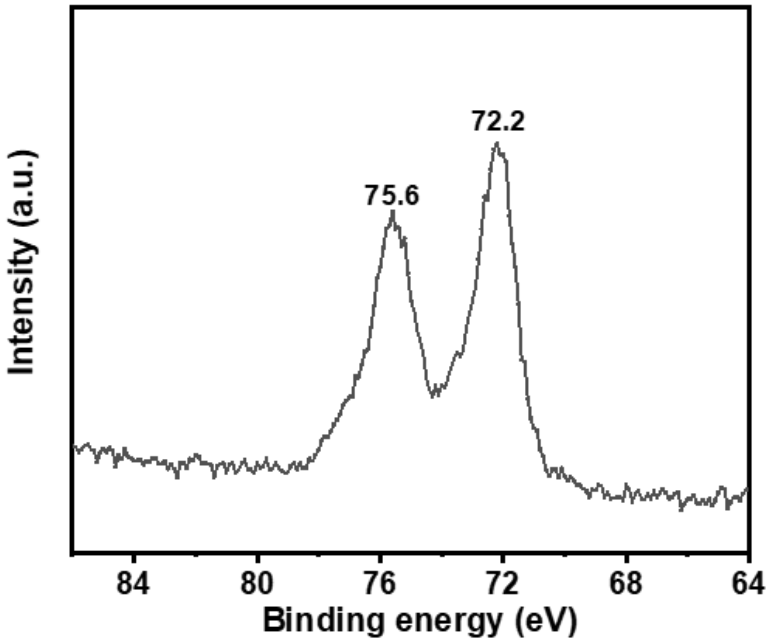

Figure S11. Related to Figure 2. The Pt 4f XPS spectra of Pt_s-CeO_2 after 504-hours methanol dehydrogenation.

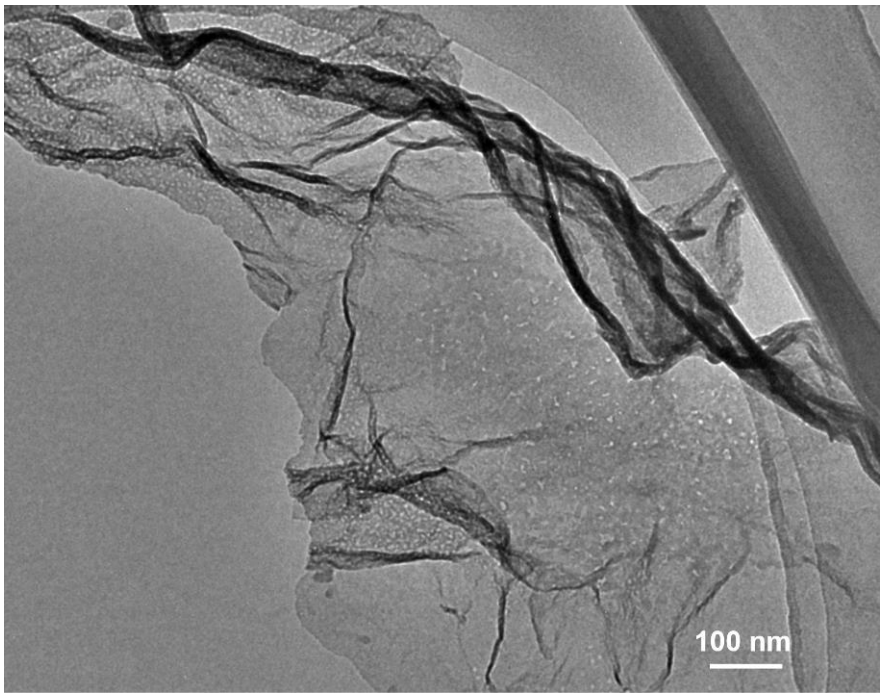

Figure S12. Related to Figure 2. The TEM image of Pt_s-CeO_2 after 504-hours methanol dehydrogenation.

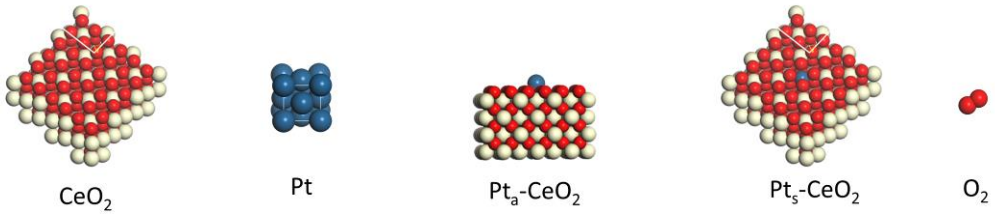

Figure S13. Related to Figure 2. The atomic structures of used for calculating the formation energy of Pt single atoms in Pt_s-CeO_2 and Pt_a-CeO_2.

The formation energy (E_f) of per Pt in Pt_s-CeO_2 was calculated by the equation of

$$E_f = E_{Pts\text{-}CeO2} - (E_{CeO2} + E_{Pt}/14 – (E_{CeO2}/72 - E_{O2}/2))$$

The formation energy (E_f) of per Pt in Pt_a-CeO_2 was calculated by the equation of

$$E_f = E_{Pta\text{-}CeO2} - (E_{CeO2} + E_{Pt}/14)$$

In the equations, $E_{Pts\text{-}CeO2}$, $E_{Pta\text{-}CeO2}$, E_{CeO2}, E_{Pt}, $E_{Pt14/CeO2}$ and E_{O2} were the total energies of slabs shown in Figure S13. The cleave surface model was CeO_2 (100). As shown in Figure S8, the CeO_2 had 72 Ce and 144 O, where 54 Ce and 108 O atoms were fixed; the Pt had 14 Pt atoms, and 9 of them were fixed; Pt_{14}/CeO_2 had 14 Pt, 72Ce, 144 O atoms, where 9 Pt, 54Ce and 108 O atoms were fixed; the Pt_s-CeO_2 had 1 Pt, 71 Ce and 144 O atoms, of which 54 Ce and 108 O atoms were fixed; the Pt_a-CeO_2 had 1 Pt, 72 Ce and 144 O atoms, of which 54 Ce and 108 O atoms were fixed; the O_2 was a free O_2 molecule.

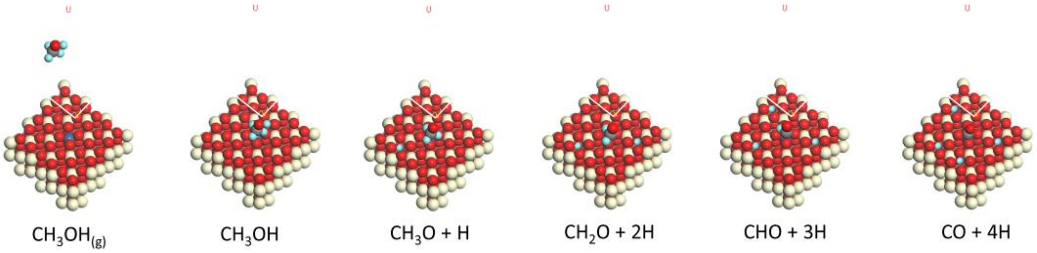

Figure S14. Related to Figure 2. The atomic structures of methanol decomposition on Pt_s-CeO_2 (100).

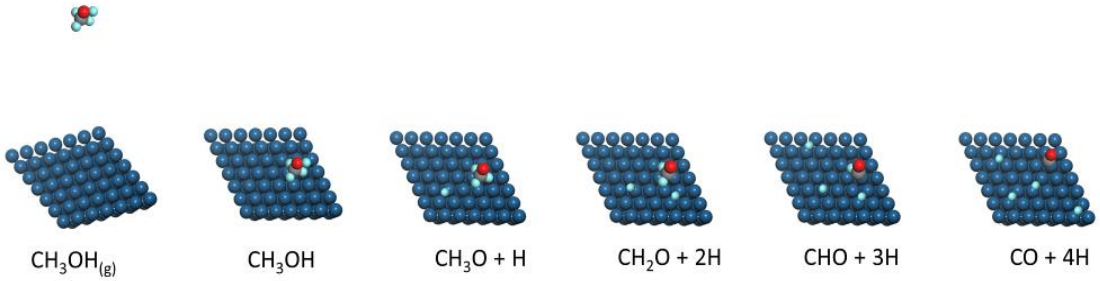

Figure S15. Related to Figure 2. The atomic structures of methanol decomposition on Pt (111) surface.

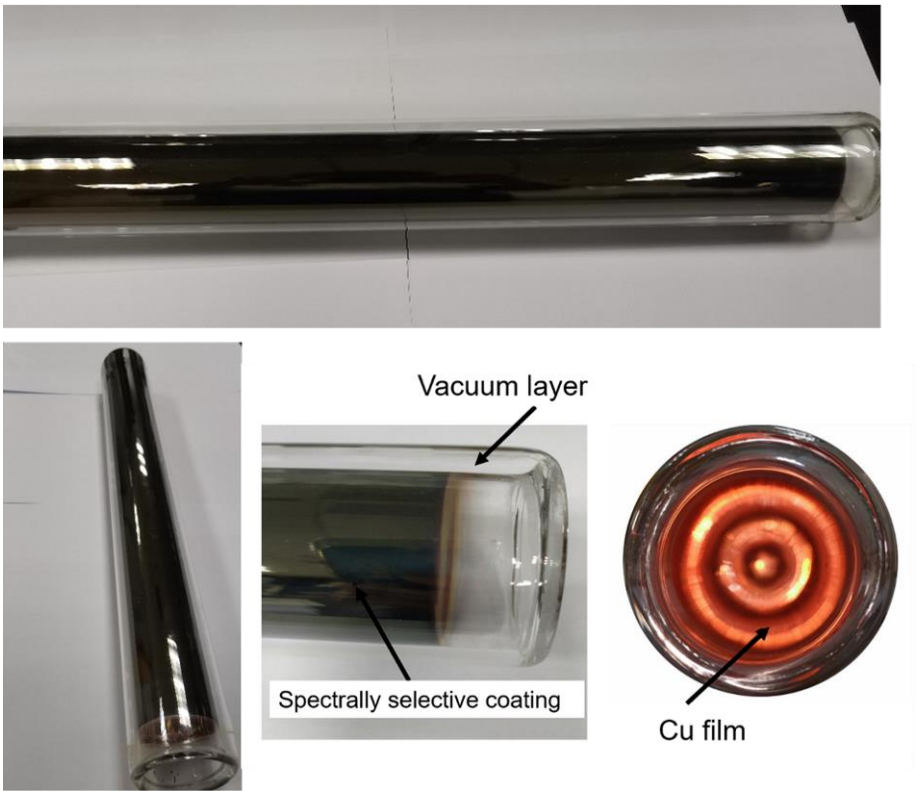

Figure S16. Related to Figure 3. Photograph of new photothermal device illustrated in Figure 3A.

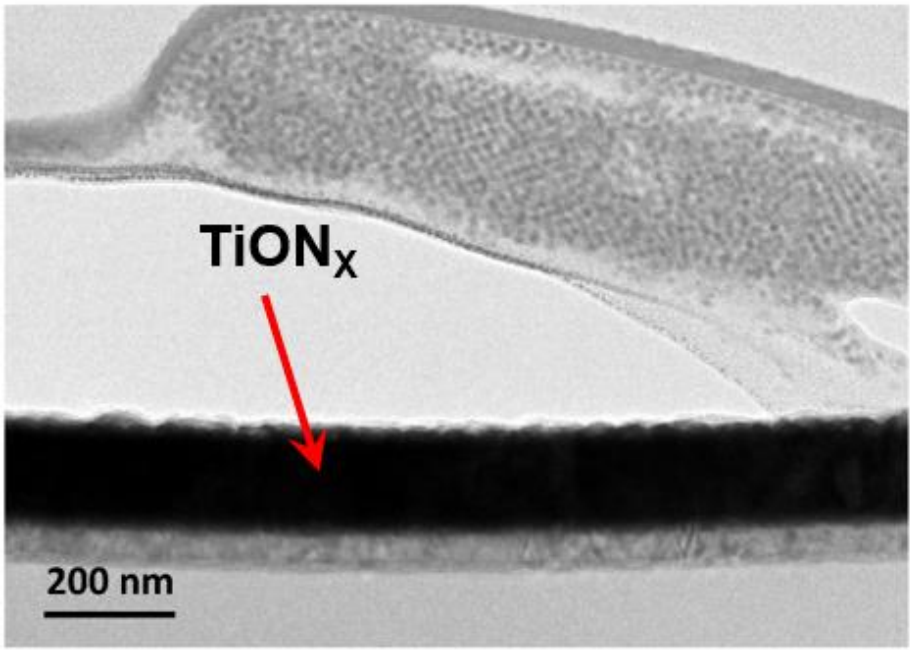

Figure S17. Related to Figure 3. TEM image of $TiON_X$.

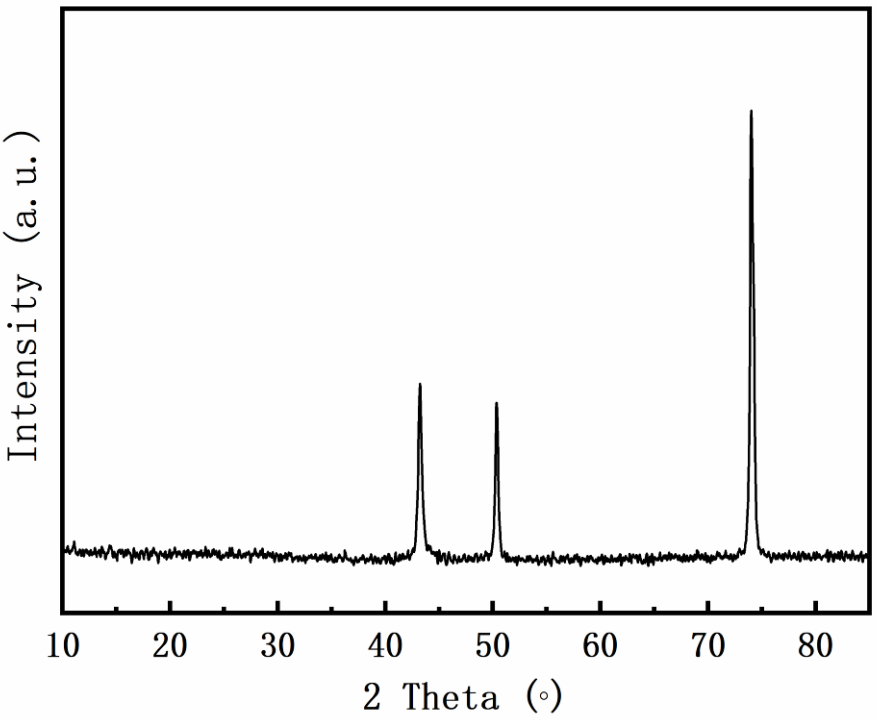

Figure S18. Related to Figure 3. XRD pattern of $TiON_x$.

Figure S19. Related to Figure 3. Photograph of graphene foam.

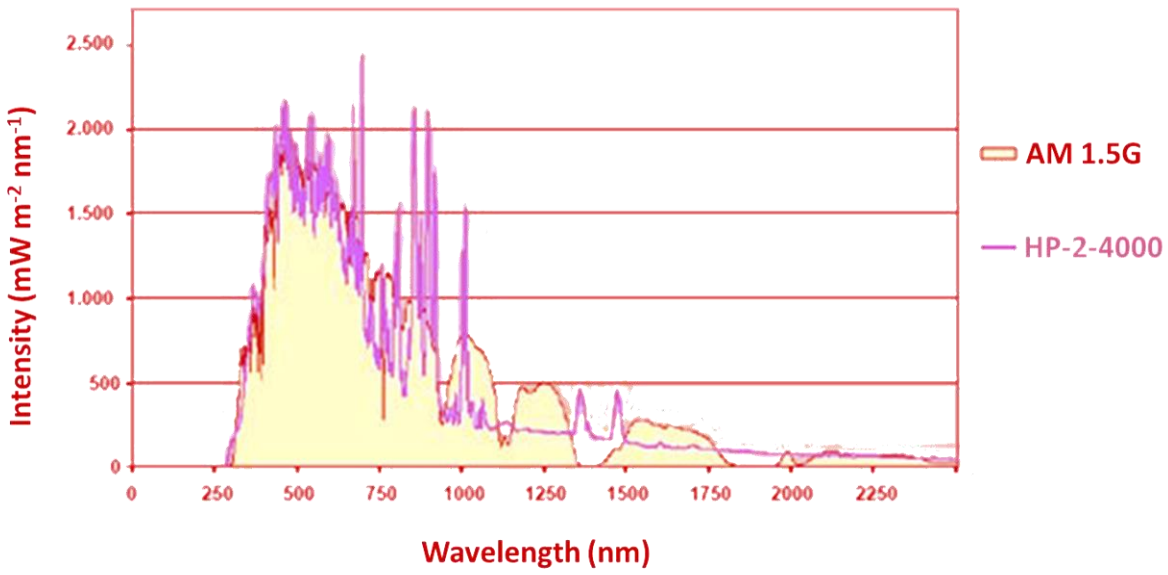

Figure S20. Related to Figure 4. The light spectrum of HP-2-4000. The spectrum of HP-2-4000 in UV-VIS region (250-800 nm) is very similar to that of AM 1.5G, while the parts of spectrum in 800-1000 nm are heightened and the parts of spectrum in IR light (λ > 1000 nm) are missing. However, we think that the difference between the spectrum of HP-2-4000 and AM 1.5G cannot significantly affect the results in this manuscript, because the missing IR light in the spectrum of HP-2-4000 is actually not conducive to photothermal conversion.

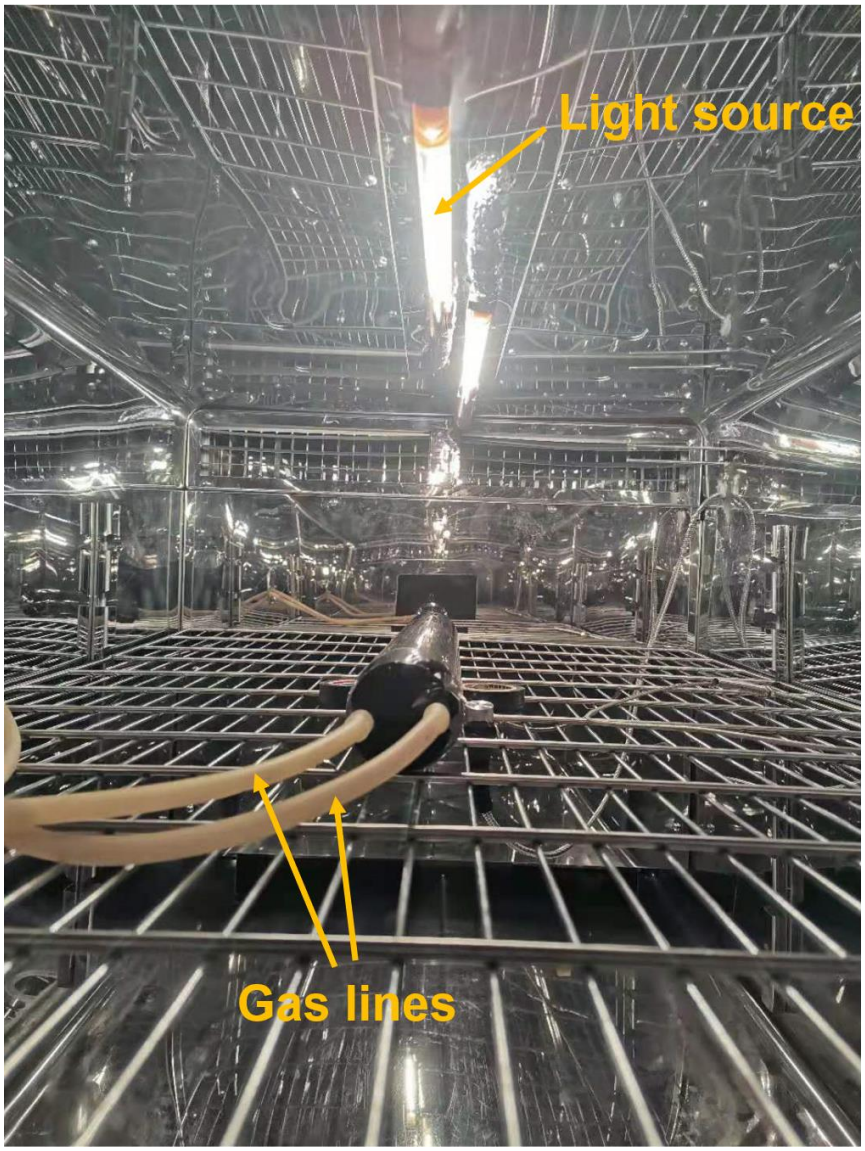

Figure S21. Related to Figure 4. The photo of the entire photothermal setup.

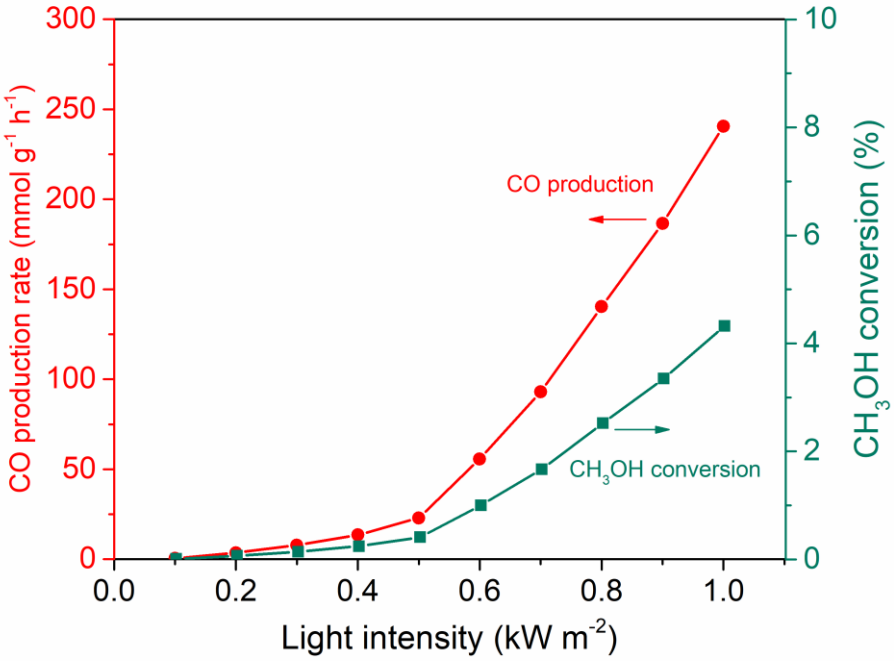

Figure S22. Related to Figure 4. CO production rate and methanol conversion of Pt_s-CeO_2 + device under different sunlight irradiations.

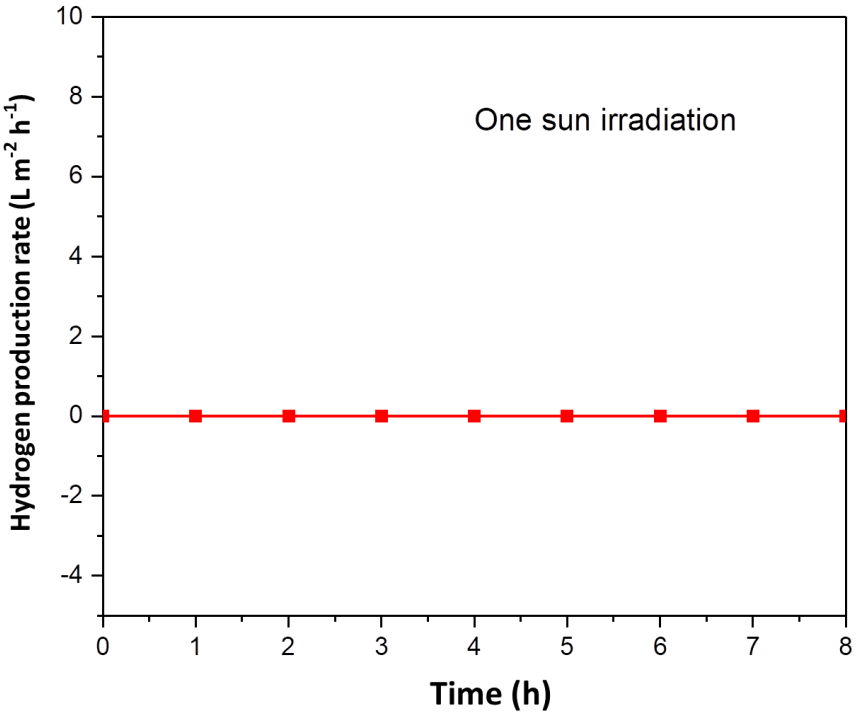

Figure S23. Related to Figure 4. Hydrogen generation rate from methanol over Pt_s-CeO_2 loaded in quartz tube under one sun irradiation.

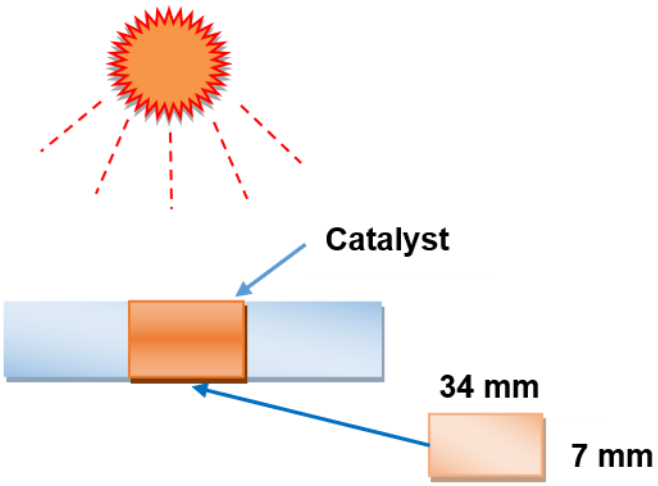

Irradiated area = 0.034×0.007 = 0.00024 m^2

Figure S24. Related to Figure 4. The irradiated area of catalyst powder in photothermal methanol dehydrogenation. It should be noted that the irradiated area coated with catalyst may absorb heat from the other area of Cu-coated quartz exposed to sunlight yet without catalyst coverage.

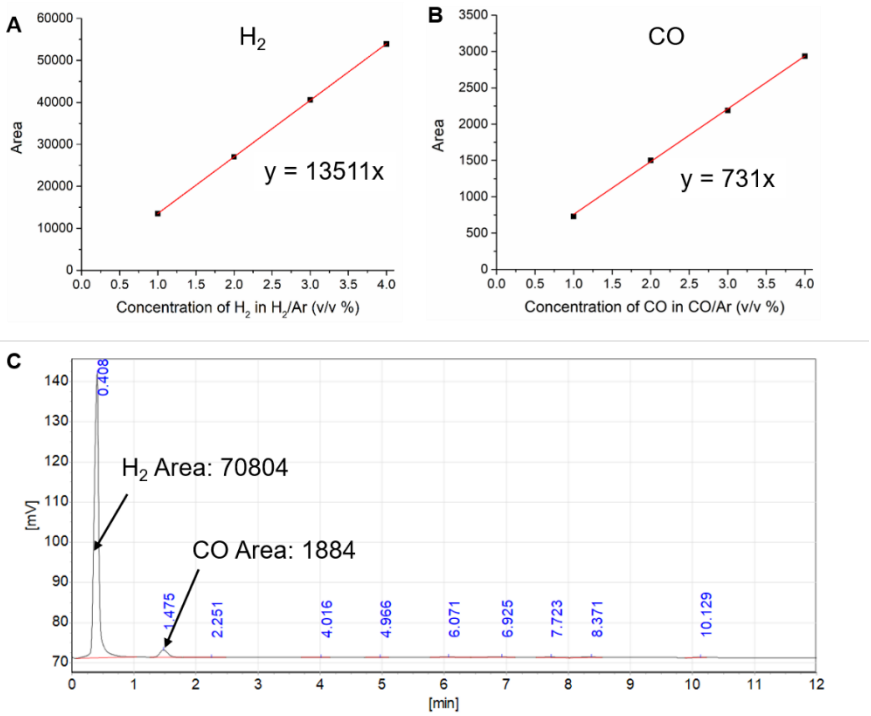

Figure S25. **Related to Figure 4.** The calibration curve of H_2 (A) and CO (B). C. The GC curve of Pt_s-CeO_2 in methanol dehydrogenation reaction under 1.0 kW·m^{-2} of sunlight irradiation.

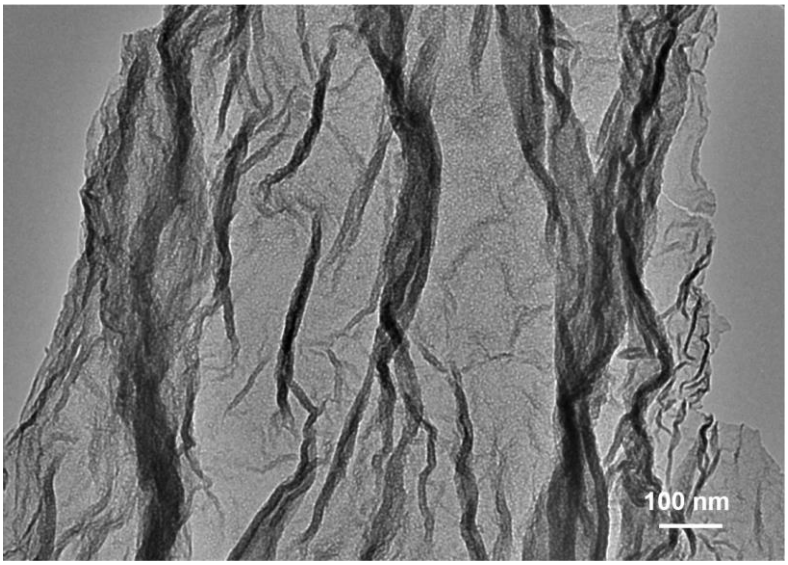

Figure S26. Related to Figure 4. The TEM image of Pt_s-CeO_2 after 744-hours photothermal methanol dehydrogenation.

Table S1. EXAFS fitting parameters of Pt from Pt_s-CeO_2 and Pt_a-CeO_2 extracted from the Pt L_3-edge. CN was the coordination number. σ^2 is the Debye–Waller factor to account for both thermal and structural disorders. R was the distance between absorber and backscatter atoms. ΔE_0 was the inner potential correction. **Related to Figure 1.**

sample	Path	CN	σ^2(10^{-3} Å^2)	R(Å)	ΔE_0(eV)
Pt_s-CeO_2	Pt-Pt				7.1
	Pt-O	7.3	9.3	2.02	
Pt_a-CeO_2	Pt-Pt				6.7
	Pt-O	4.9	7.5	1.99	

Table S2. The ICP-AES data of Pt_s-CeO_2. The actual atomic ratio of Pt to Ce is estimated to be 7.2 at.% , which is almost the same as the theoretical value (7.1 at.%). Measurement condition: The catalyst was dissolved by 4 M HNO_3 at 150 °C for 6 hours; ICP model: Thermo ICAP 6300. **Related to Figure 1.**

Analyte	Concentration (mg L^{-1})[a]	RSD[a]
Pt	0.057	1.02 %
Ce	0.570	0.36 %

[a]Relative standard deviation

Table S3. Comparison of solar-to-fuel conversion efficiency in solar-driven catalytic reactions. **Related to Figure 4.**

Entry	Reaction	Light source	Solar-to-fuel conversion efficiency	Ref.
1	$CH_3OH \rightarrow 2H_2 + CO$	Simulated AM 1.5G illumination at 1 Sun	32.9%	This work
2	$CO + H_2O \rightarrow H_2 + CO_2$	300 W Xe lamp illumination at 8.5 Suns	1.1%	(Zhao et al., 2019)
3	$CH_4 + CO_2 \rightarrow 2H_2 + 2CO$	500 W Xe lamp illumination at 343.6 Suns	10.3%	(Huang et al., 2018)
4	$CH_4 + CO_2 \rightarrow 2H_2 + 2CO$	500 W Xe lamp illumination at 371.1 Suns	12.5%	(Li et al., 2018)
5	$C_2H_5OH \rightarrow H_2 + CH_3CHO$	Simulated AM 1.5G illumination at 5.7 Suns	3.8 %	(Luo et al., 2020)

Supplemental References

Blöchl, P.E. (1994). Projector augmented-wave method. Physi. Rev. B *50*, 17953-17979.

Chen, J., Yao, B., Li, C., and Shi, G. (2013). An improved Hummers method for eco-friendly synthesis of graphene oxide. Carbon *64*, 225-229.

Grimme, S., Antony, J., Ehrlich, S., and Krieg, H. (2010). A consistent and accurate ab initio parametrization of density functional dispersion correction (DFT-D) for the 94 elements H-Pu. J.Chem. Phys. *132*, 154104.

Henkelman, G., Uberuaga, B.P., and Jonsson, H. (2000). A climbing image nudged elastic band method for finding saddle points and minimum energy paths. J. Chem. Phys. *113*, 9901-9904.

Huang, H., Mao, M., Zhang, Q., Li, Y., Bai, J., Yang, Y., Zeng, M., and Zhao, X. (2018). Solar‐Light‐Driven CO_2 Reduction by CH_4 on Silica‐Cluster‐Modified Ni Nanocrystals with a High Solar‐to‐Fuel Efficiency and Excellent Durability. Adv. Energy Mater. *8*, 1702472.

Kresse, G., and Joubert, D. (1999). From ultrasoft pseudopotentials to the projector augmented-wave method. Phys. Rev. B *59*, 1758-1775.

Li, Y., Mao, M., Zhang, Q., Yang, Y., Huang, H., Jiang, Z., Hu, Q., and Zhao, X. (2018). Solar-light-driven CO_2 reduction by methane on Pt nanocrystals partially embedded in mesoporous CeO_2 nanorods with high light-to-fuel efficiency. Green Chem. *20*, 2857-2869.

Luo, S., Song, H., Philo, D., Oshikiri, M., and Ye, J. (2020). Solar-driven production of hydrogen and acetaldehyde from ethanol on Ni-Cu bimetallic catalysts with solar-to-fuels conversion efficiency up to 3.8%. Appl. Catal. B-Environ. *272*, 118965.

Perdew, J.P., Burke, K., and Ernzerhof, M. (1996). Generalized Gradient Approximation Made Simple. Phys. Rev. Lett. *77*, 3865-3868.

Zhao, L., Qi, Y., Song, L., Ning, S., Ouyang, S., Xu, H., and Ye, J. (2019). Solar-Driven Water–Gas Shift Reaction over CuOx/Al2O3 with 1.1 % of Light-to-Energy Storage. Angew. Chem. Int. Ed. *58*, 7708-7712.